Abstract

Title: LASER BEAM PROPAGATION THROUGH SCATTERING MEDIUM FOR SUB-SURFACE LASER DOSIMETRY

Renee D. Naphas, Master of Science, 2011

Thesis Directed by: Dr. Yu Chen
Departent of Bioengineering

Dr. Ilko Ilev
Food and Drug Administration

Optical therapeutic (OT) devices, which range in applications from laser tissue ablation and surgery to photodynamic (PDT) and low-level laser therapies (LLLT), are assessed for safety and efficacy on the basis of Maximum Permissible Exposure (MPE), which measures radiation dose in J/cm^2, delivered to the target area as well as surrounding tissues. We present the characterization of an imaging system for, and method of, determining the maximum dose of devices capable of delivering peak energy level to sub-surface tissue layers. This method utilizes a fiber optic based imaging system designed to allow for comparability across laser parameters, tissue sample type and layer thickness.

LASER BEAM PROPAGATION THROUGH SCATTERING MEDIUM FOR SUB-SURFACE LASER DOSIMETRY

by

Renee D. Naphas

Thesis submitted to the Faculty of the Graduate School of the
University of Maryland, College Park in partial fulfillment
of the requirements for the degree of
Maser of Science
2011

Advisory Committee

Professor Yu Chen, Chair
Professor Ilko Ilev
Professor Julius Goldhar

Acknowledgements

I would like to thank my advisor Professor Yu Chen for his support and direction throughout my time at the university. I deeply admire, and strive to emulate, his unbreakably calm perseverance and dedication to excellence.

I sincerely thank Dr. Ilko Ilev for motivating me with his contagious enthusiasm and bringing his extensive experience in the field to every step of this project.

I would also like to thank the professors serving on my thesis committee: Profs. Yu Chen, Ilko Ilev and Julius Goldhar.

My friends and family have my heartfelt gratitude for their support, encouragement, love, and of course never ending cups of tea over the years.

List of Tables

List of Figures

CHAPTER 1 INTRODUCTION

Optical therapeutics (OT) is an emerging field of modern biophotonics that is increasingly being applied in various vast areas of life sciences and biomedicine ranging from laser tissue ablation and surgery to photodynamic (PDT) and low-level laser therapies (LLLT). To gain FDA approved/cleared status, OT devices are evaluated for safety and efficacy in compliance with the FDA recognized guidance documents and standards. The efficient laser radiation dose (or dose) level is heavily dependent on treatment goals and is determined by comprehensive scientific studies including *in-vitro*, *in-vivo* and clinical trials. The American National Standards Institute (ANSI) defines safe dose standards for laser therapeutics devices used on skin or retina in terms of Maximum Permissible Exposure (MPE) [1][2][3]. These standards are in the form of MPE charts that list safe laser radiation doses based on various laser parameters (such as power, wavelength, repetition rate, spot diameter, and focal length) for both types of tissue. Independent studies were conducted to establish and verify the MPE levels listed in the safety standards. Companies with devices under review must submit experimental and analytical data, and evaluation analysis to verify that their device's output meets safety standards at standard and maximum operation levels as well as within the claimed effective range. However, this is only possible for devices that reach their highest intensities at the tissue surface.

Currently no standards exist for devices with a subsurface focal point. For these devices animal tissue (*ex-vivo* and *in-vivo*) and human (clinical or cadaver) trials for adverse effects are the only means of evaluating device safety. The creation of guidance and/or standard documents for subsurface light-tissue interactions would dramatically

reduce the need for animal and human testing, ensure uniformity in device testing and safety, and reduce the amount of time for device approval.

Extensive testing of focused laser beams across laser parameters, tissues, and tissue thicknesses is required for the creation of enforceable safety standard procedures for focused laser therapy devices for sub-dermal tissues. The same testing method could be used to determine the dose of an OT technique or device at any level of any tissue, therefore allowing companies to meet FDA requirements with fewer and less invasive experiments. To accomplish this, a test method must first be proven accurate and repeatable across all variations.

In this thesis, we present a proof-of-concept testing method. Motivated by considerations for measuring sub-dermal OT dose, including LLLT and PDT dose, for the determination of safety standards as well as device safety and efficacy verification, we designed a measurement system and process. The fiber optic-based evaluation device has the potential to be incorporated into a needle assembly for minimally invasive *ex-vivo* and *in-vivo* implementation. We tested the limitations of the system, tested and compared measuring processes, and verified its functional viability. This work will not address the determination of effective or safe dose levels for any type of treatment or tissue; it will address a method of determining a device's capability to deliver a specified dose to sub-dermal tissues with a focused or collimated laser beam, which is required for efficacy and safety evaluations of OT techniques and devices.

Chapter 2 outlines proposed OT evaluation and study systems and methods, aspects of which are the focus of experimentation and modeling discussed in subsequent chapters. Discussions focus on detection system developmental considerations and limitations.

Chapter 3 describes a calibration method used to verify the validity of the proposed dose measuring systems. We discuss sources of power attenuation and derive theoretical models of expected beam profiles. These models are compared to experimental measurements taken in various sample media.

Chapter 4 focuses on system range of motion and detector limitations. Scanning methods are compared experimentally to find a method that can overcome limitations. We develop theoretical models of fiber numerical aperture induced acceptance angle limitations and ideal beam profiles for each input divergent beam (meant to approximate scattering by tissue). Theoretical models are taken into consideration along with experimental data to determine the optimal profile scanning method.

CHAPTER 2 PROPOSED LASER THERAPY DEVICE SAFETY AND EFFICACY TESTING METHOD

For this thesis, we conducted experiments with the intent to validate a proposed method of determining an OT's dose at various tissue depths. The test methods and devices outlined in this chapter are proposed future developments and were only considered theoretically to direct experimentation; they were not fully developed as a part of this research. All experiments included in this study were created with the goal of verifying the viability of the proposed devices and methods, which were considered as the ultimate goal of this area of research. In this Chapter, we describe the proposed testing methods and devices, the advantages and implementation challenges of each, and the means by which we addressed each concern.

Section 2.1 Definition of Dose

All experiments and proposed methods and devices must determine laser radiation dose (or dose). Dose is a commonly used term in the areas of photobiology, photochemistry and optical therapeutics including LLLT, PDT, laser tissue ablation and surgery, and light-tissue interactions. In these areas, the dose is defined and utilized as the conventionally utilized quantity radiant exposure, and it has the same units of J/cm^2. [4]Dose is defined as:

$$\text{Dose}\,[J/m^2] = \frac{\text{Power}\,[W]}{\text{Area}\,[m^2]}\,\text{Exposure Time}\,[s], \qquad \textbf{Equation 1}$$

where Area is defined as the cross-sectional area of the beam at the $1/e^2$ beam diameter and the Power is the total power integrated over Area at a given position. A beam profile must be obtained to determine the $1/e^2$ beam diameter (from which Area is calculated in

all cases in this thesis because all beams used were Gaussian). The experiments of this thesis focus on verifying the ability of a process or device to accurately calculate dose by determining Power and a beam profile at various tissue depths.

The typical progression of verification of biomedical device testing dictates the use of samples in the following order:

1. Tissue Phantom
2. *Ex-vivo* Tissue Samples
3. *In-vivo* Tissue Samples

Experiments involving each of these sample types present their own challenges and often involve the use of different detection systems. However, we intend to outline a measurement process usable across all sample types. It should allow for comparisons across data sets while limiting variations and providing a single testing system and method usable for any OT device. Therefore we first considered the most complicated process, *in-vivo* tissue measurements, and imposed the limitations thereof on all testing, regardless of sample type.

Section 2.2 *In-vivo* Tissue Testing

We propose that a minimally invasive needle based fiber-optic detector, suitable for use in living human beings, would provide dose measurements sufficient for regulatory safety standard determination and compliance verification. This device is illustrated in Figure 1. The use of an optical fiber allows measurements to be taken at any tissue depth within reach of a needle. At present, typical OT devices are only capable of radiating to a depth of at most a few millimeters[5][6], which is well within reach of a biopsy needle. We performed experiments using an optical fiber as the detector, as dictated by the need for minimally invasive *in-vivo* testing.

It may be difficult to measure the exact depth of a fiber within tissue or to compare *in-vivo* measurements from different needle positions even if the depth is determined to be essentially identical due to the high variability of biological cellular structures. By using an optical fiber, beam parameters, such as wavelength or power, may be varied without moving the detection device. This method allows for the study of laser beam propagation through tissue across any variety of beam parameters simultaneously. It also produces results legitimately comparable for any biological tissue, regardless of structure variability, even without statistical averaging, which is necessary to study the effects of OT on fine biological structures.

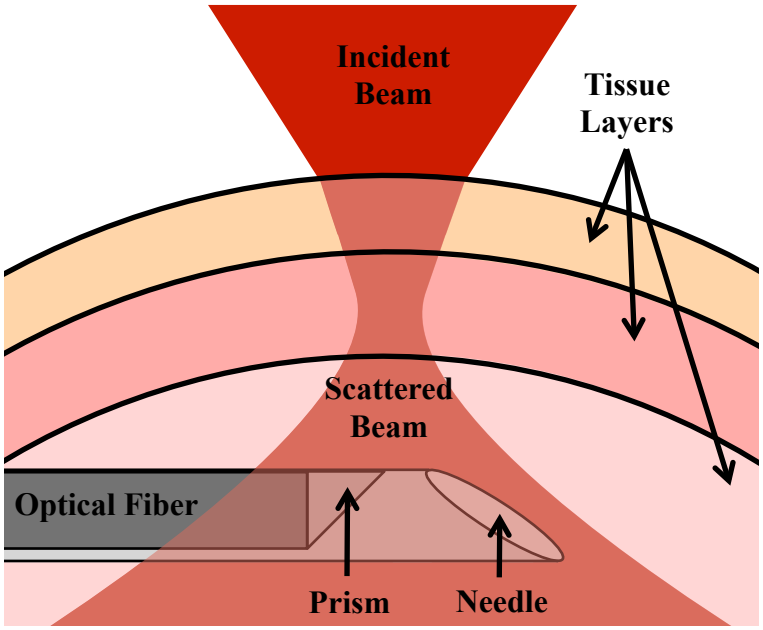

Figure 1: Illustration of proposed needle based *in-vivo* dose measurement device. Light is directed into the optical fiber via a prism. Several experiments discussed in this thesis were performed as preliminary proof-of-concept verification for this end goal device.

Section 2.3 *Ex-Vivo* Tissue Testing

The use of *ex-vivo* tissue samples is not only a precursory step to the use of *in-vivo* tissues, it can also be used in studies deemed excessively invasive for *in-vivo* experimentation to gather more and/or different information (for example, to study vital organs). We propose that thin slices of tissue samples can be used to provide two-dimensional images of beam profiles. The images can be obtained for various types of tissues, tissue thicknesses, or tissue combinations and used to determine dose as well as study the effects of off-axis scattering or focusing due to biological cellular structures. Figure 2 illustrates a possible scanning technique and dose determination method.

The advantages discussed in Section 2.2 and the limitations of *in-vivo* experimentation dictate the use of an optical fiber detector. By using an optical fiber for *ex-vivo* measurements as well, we maintain continuity across experiments, which allows for easier result comparisons and validity verification. Scanning a fiber along lines, such a_1 and a_2, at intervals along the y-axis could create profile images #1 and #2 shown in Figure 2.

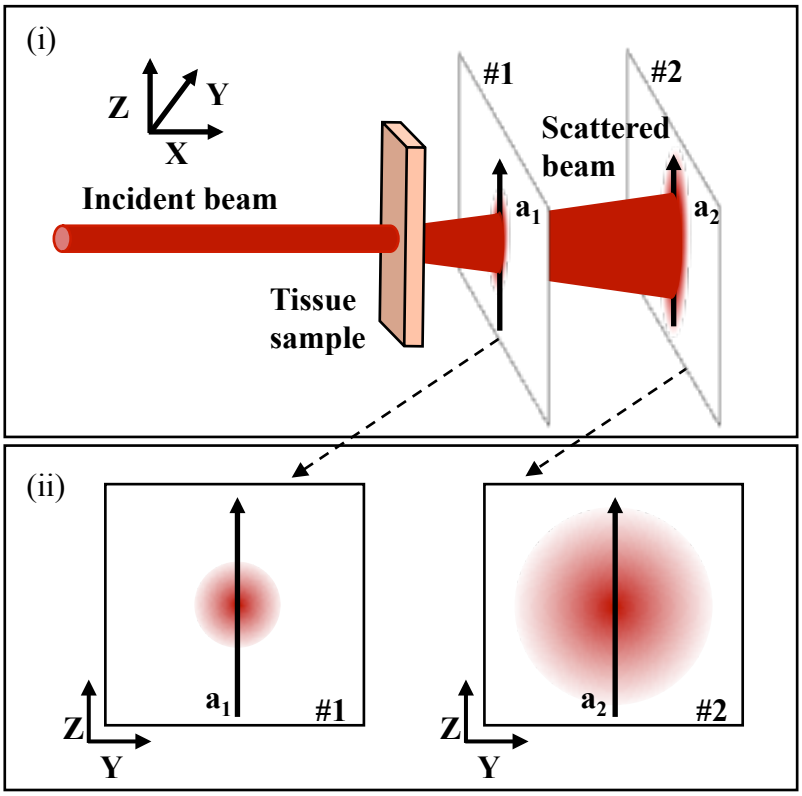

Figure 2: Illustration of linear 2-D scanning of beam profiles of laser light scattered through a thin tissue sample. The beam profiles, #1 and #2, represent measurements taken at two different distances from the tissue sample. The dispersion angle calculated using these two profiles (calculated using the beam widths measured along lines a_1 and a_2) would be used to extrapolate the dose at the point that the light exits the back of the tissue sample, where system limitations prevent image scanning.

Section 2.4 Tissue Phantom Testing

Tissue phantoms are often used as a precursory experimental step to verify methods and hypotheses before using tissue samples (*ex-vivo* or *in-vivo*). For the proposed *ex-vivo* imaging system, solid tissue phantoms could be used to demonstrate the fiber scanning method validity. A liquid phantom could be used for a preliminary calibration before progressing to *in-vivo* experiments. As in previously discussed cases, an optical fiber detector should also be utilized for all tissue phantom experiments.

Section 2.5 System Calibration Feasibility

To verify that a fiber optic based system can be calibrated for use in air (as would be the case for *ex-vivo* tissue scans) and in direct contact with a sample (as for *in-vivo* testing), we scanned beam profiles in air and a liquid tissue phantom. The liquid sample required a containment vat; therefore we took all measurements within the confines of the vat regardless of sample medium so that successive measurements could be taken without changing the position of the fiber. In Chapter 3 we develop and theoretically verify a calibration process for a fiber optic dose measurement system. While beam width measurements can be made with power readings in arbitrary units, an accurate power measurement at a single point, the peak of the profile, is required to determine dose. We used optical fiber and direct photo detector measurements to derive a calibration factor to determine accurate beam peak power.

Section 2.6 System Limitations and Scan Path Considerations

Both the use of an optical fiber as a detector and the process of taking measurements within the confines of a vat impose system detection angle and range of motion limitations. Chapter 4 focuses on the determination of system limitations and optimal scanning method.

Optical fiber is limited in its acceptance angle by its numerical aperture. We develop and compare two possible scanning methods to determine the extent of this limitation, and to determine the optimal path along which to scan the fiber to account for it: either a linear or rotational path. Each of these paths has limiting factors that we model and use to compare to experimental measurements taken using a lens to create a divergent beam,

which approximates scattering in tissue while maintaining radial uniformity. Results from linear and rotational scans are compared across various source divergence angles and in various media to assess the effects of the numerical aperture of the detecting fiber on measured dose.

CHAPTER 3 CALIBRATION METHOD

Section 3.1 Introduction

The ultimate goal for this area of research is to have a validated method of dose measurement via readings taken *in-vivo* or *ex-vivo* with a needle based fiber optic detector, as discussed in Chapter 2. There are several steps that must be taken to calibrate such a system to prove it is a viable option. Two values need to be measured to calculate an accurate dose: area of the beam cross-section at the depth of interest and the total power delivered to that area. If only the area were needed, a measurement of power in arbitrary units would suffice. However, the exact power is necessary for an accurate dose measurement.

The system developed in this project used an optical fiber to gather irradiation within a phantom sample and deliver it to a detector. Sources of inaccuracy include: reflection at the sample/fiber interface, attenuation in the fiber, and fiber numerical aperture limitation. In the following sections we discuss the effects of the first two factors, derive theoretical correction factors, and verify an experimental calibration technique. The third source of inaccuracy, related to numerical aperture, is addressed in Chapter 4.

Section 3.2 discusses and derives reflection and transmission at the fiber's detecting surface.

Section 3.3 discusses experiments done to determine the transmission coefficient of the fiber.

Section 3.4 discusses fiber loss mechanisms other than reflection.

Section 3.5 discusses an experimentally tested method for calibration factor determination to account for power loss.

Section 3.2 Reflection/Transmission at the Detecting Fiber

When a wave meets the boundary between two linear media it gives rise to a reflected and transmitted wave. The proportion of the initial power that is transmitted is dependent upon the refractive indices of the media, the incident angle at which the wave meets the boundary, and the polarization of the incoming wave. These factors and their associated coefficients will be discussed and derived in the following sections.

Section 3.2.1 Plane Waves in a Non-Conducting Medium

Traveling wave solutions for the transport of electromagnetic energy can be derived from Maxwell's equations:

$$\nabla \cdot \bar{B} = 0, \qquad \textbf{Equation 2}$$

$$\nabla \cdot \bar{D} = 0, \qquad \textbf{Equation 3}$$

$$\nabla \times \bar{E} + \frac{\partial \bar{B}}{\partial t} = 0, \qquad \textbf{Equation 4}$$

$$\nabla \times \bar{H} - \frac{\partial \bar{D}}{\partial t} = 0, \qquad \textbf{Equation 5}$$

where $\bar{B}$ is magnetic field, $\bar{E}$ is the electric field, $\bar{D}$ is the electric displacement, $\bar{H}$ is the magnetic field strength, and t is time. The electromagnetic waves of interest are transverse plane waves, traveling in a uniform isotropic medium with harmonic time dependent solutions. Therefore, assuming $\bar{D} = \varepsilon \bar{E}$, $\bar{B} = \mu \bar{H}$, and that the time

dependence is $e^{-i\varpi t}$, where ε is permittivity, μ is permeability and ϖ is frequency. Equations 2-5 can be written as

$$\nabla \cdot \overline{B} = 0, \qquad \textbf{Equation 6}$$

$$\nabla \cdot \overline{D} = 0, \qquad \textbf{Equation 7}$$

$$\nabla \times \overline{E} - i\varpi \overline{B} = 0, \qquad \textbf{Equation 8}$$

$$\nabla \times \overline{B} + i\varpi\mu\varepsilon \overline{E} = 0. \qquad \textbf{Equation 9}$$

In this case ε and μ are assumed to be real (no loss). Combining Equations 8 and 6 results in the Helmholtz wave equation

$$(\nabla^2 + \mu\varepsilon\varpi^2)\left\{ \begin{array}{c} \overline{E} \\ \overline{B} \end{array} \right\} = 0. \qquad \textbf{Equation 10}$$

Consider a plane wave traveling in the x direction, of the form $e^{ikx-i\varpi t}$, as a possible solution to Equation 10. For this to be a solution the wave number k and frequency ϖ are requisitely related by

$$k = \sqrt{\mu\varepsilon}\varpi\,. \qquad \textbf{Equation 11}$$

From this equation the phase velocity v and the index of refraction n can be defined as

$$v = \frac{\varpi}{k} = \frac{1}{\sqrt{\mu\varepsilon}} = \frac{c}{n}, \quad n = \sqrt{\frac{\mu}{\mu_0}\frac{\varepsilon}{\varepsilon_0}}\,. \qquad \textbf{Equation 12}$$

In one dimension the plane wave solution can be written

$$u(x,t) = ae^{ikx-i\varpi t} + be^{-ikx-i\varpi t}\,. \qquad \textbf{Equation 13}$$

This solution can be rewritten, using the relation $\varpi = kv$,

$$u_k(x,t) = ae^{ik(x-vt)} + be^{-ik(x+vt)}\,. \qquad \textbf{Equation 14}$$

This solution represents two waves, superimposed, traveling in the positive and negative x directions at phase velocity v. For the three-dimensional case the wave vector is defined as $\bar{k} = k\hat{n}$, where $\hat{n}$ is the constant unit vector of the direction propagation of the traveling wave. Applying the constraints of Equation 10, the equations of the plane wave fields can be written as

$$\bar{E}(\bar{x},t) = \bar{\mathscr{E}} e^{ik\hat{n}\cdot\bar{x}-i\varpi t} \qquad \textbf{Equation 15}$$

$$\bar{B}(\bar{x},t) = \bar{\mathscr{B}} e^{ik\hat{n}\cdot\bar{x}-i\varpi t} \qquad \textbf{Equation 16}$$

where $\bar{E}$ and $\bar{B}$ are both orthogonal to $\hat{n}$ and $\bar{\mathscr{E}}$ and $\bar{\mathscr{B}}$ are constant field strength vectors restricted by $\bar{\mathscr{B}} = \sqrt{\mu\varepsilon}\hat{n} \times \bar{\mathscr{E}}$.

$\bar{\mathscr{E}}$ can be written as $\bar{\mathscr{E}} = \hat{\varepsilon}_1 E_1 + \hat{\varepsilon}_2 E_2$, which is the most general homogeneous plane wave equation. In this equation, $\hat{\varepsilon}_1, \hat{\varepsilon}_2$ and $\hat{n}$ form a set of mutually orthogonal unit vectors and amplitudes E_1 and E_2 are complex numbers, between which any phase difference signifies a polarization other than linear.

Section 3.2.2 Reflection and Transmission of Electromagnetic Waves at a Dielectric Interface

Section 3.2.2.1 Boundary Conditions

The boundary conditions at the interface between linear mediums 1 and 2, which is assumed to be free of charge or current, demand that: the normal components of the magnetic induction and electric displacement are continuous across the surface of discontinuity and the tangential components of the electric vector and the magnetic vector are also continuous across the boundary

$$\left.\begin{aligned}\hat{n}\cdot(\overline{B}_2-\overline{B}_1)=0,\hat{n}\cdot(\overline{D}_2-\overline{D}_1)=0\\ \hat{n}\times(\overline{H}_2-\overline{H}_1)=0,\hat{n}\times(\overline{E}_2-\overline{E}_1)=0\end{aligned}\right\}. \quad \textbf{Equation 17}$$

In the presence of a charge or current at the boundary a discontinuity would exist for the normal component of electric displacement and the tangential component of the magnetic vector, but this case does not need to be considered for this application.

Section 3.2.2.2 Reflection and Transmission at Oblique Incidence

Suppose that a monochromatic plane wave approaches an interface between two homogeneous media of different optical properties; in this case incident electric and magnetic fields

$$\overline{E}_i(\overline{r},t)=\overline{\mathscr{E}}_i e^{i(\overline{k}_i\cdot\overline{r}-\varpi t)} \text{ and } \overline{B}_i(\overline{r},t)=\frac{1}{v_1}(\hat{k}_i\times\overline{E}_i), \quad \textbf{Equation 18}$$

give rise to a reflected wave

$$\overline{E}_R(\overline{r},t)=\overline{\mathscr{E}}_R e^{i(\overline{k}_R\cdot\overline{r}-\varpi t)} \text{ and } \overline{B}_R(\overline{r},t)=\frac{1}{v_1}(\hat{k}_R\times\overline{E}_R) \quad \textbf{Equation 19}$$

and a transmitted wave

$$\overline{E}_T(\overline{r},t)=\overline{\mathscr{E}}_T e^{i(\overline{k}_T\cdot\overline{r}-\varpi t)} \text{ and } \overline{B}_T(\overline{r},t)=\frac{1}{v_2}(\hat{k}_T\times\overline{E}_T). \quad \textbf{Equation 20}$$

These three wave field equations can be combined using the boundary conditions given in Equation 17 along with the fact that all three waves have the same frequency to draw the following conclusions:

1. The plane of incidence can be defined as the plane formed by the incident, reflected and transmitted wave vectors. (In Figure 3, this is the x-z plane)

$$k_i Sin(\theta_i)=k_R Sin(\theta_R)=k_T Sin(\theta_T) \quad \textbf{Equation 21}$$

$$\theta_i = \theta_R \text{ and } \frac{Sin(\theta_T)}{Sin(\theta_i)} = \frac{n_1}{n_2} \text{ (Snell's Law)} \qquad \textbf{Equation 22}$$

therefore

2. Given the geometry defined in Figure 3, the boundary conditions become:

$$\left.\begin{aligned} &\varepsilon_1(\bar{\mathscr{E}}_i + \bar{\mathscr{E}}_R)_z = \varepsilon_2(\bar{\mathscr{E}}_T)_z \\ &(\bar{\mathscr{B}}_i + \bar{\mathscr{B}}_R)_z = (\bar{\mathscr{B}}_T)_z \\ &(\bar{\mathscr{E}}_i + \bar{\mathscr{E}}_R)_{x,y} = (\bar{\mathscr{E}}_T)_{x,y} \\ &(\bar{\mathscr{B}}_i + \bar{\mathscr{B}}_R)_{x,y} = \frac{1}{\mu_2}(\bar{\mathscr{B}}_T)_{x,y} \end{aligned}\right\} \qquad \textbf{Equation 23}$$

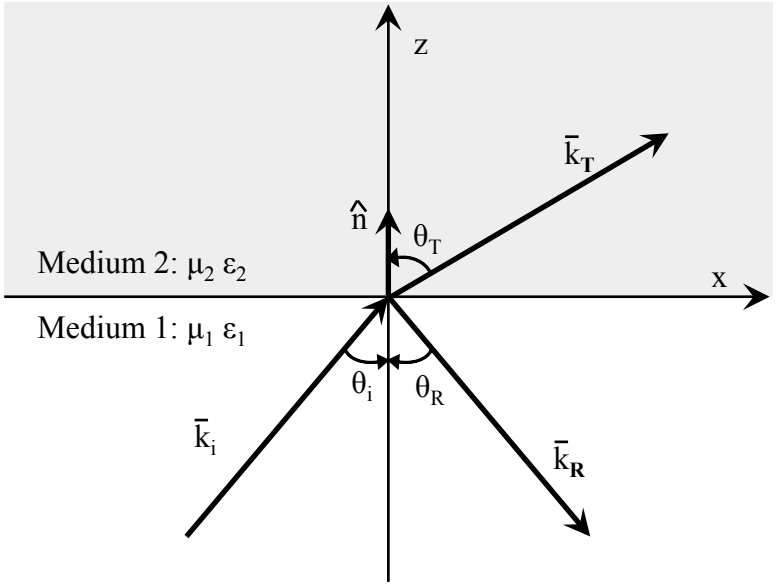

Figure 3: Wave $\bar{k}_i$, is incident on the plane formed by the $z = 0$ boundary, resulting in reflected wave $\bar{k}_R$ and transmitted wave $\bar{k}_T$.

Section 3.2.2.3 Reflection and Transmission for Parallel Polarization

There are two polarizations possible for plane waves: parallel or perpendicular to the plane of incidence. In this section we address the parallel polarization case, which is illustrated in Figure 4.

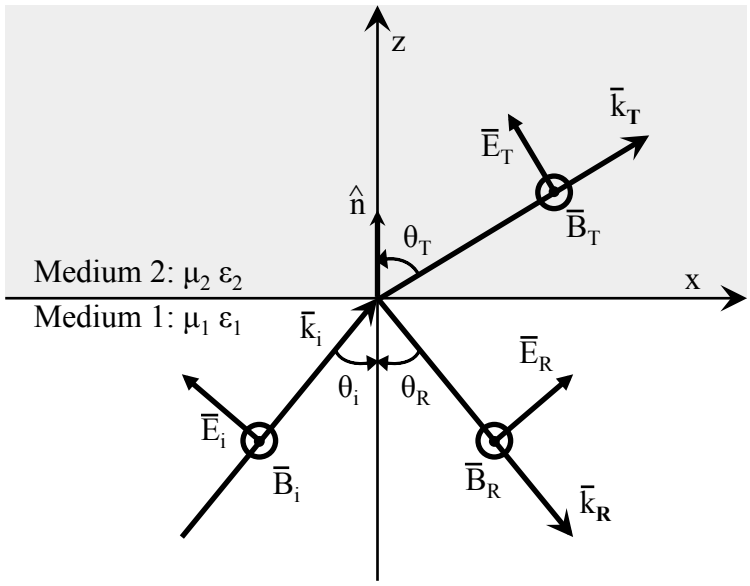

Figure 4: Wave $\bar{k}_i$, with parallel polarization, is incident on the plane formed by the $z = 0$ boundary, resulting in reflected wave $\bar{k}_R$ and transmitted wave $\bar{k}_T$.

The boundary conditions of Equation 23 are applied to the case shown in Figure 4 to produce two of Fresnel's equations

$$\bar{\mathscr{E}}_R = \frac{\alpha - \beta}{\alpha + \beta}\bar{\mathscr{E}}_i, \quad \bar{\mathscr{E}}_T = \frac{2}{\alpha + \beta}\bar{\mathscr{E}}_i \,, \qquad \textbf{Equation 24}$$

where $\alpha \equiv \dfrac{Cos(\theta_T)}{Cos(\theta_i)}$ and $\beta \equiv \dfrac{\mu_1 v_1}{\mu_2 v_2} = \dfrac{\mu_1 n_2}{\mu_2 n_1}$. **Equation 25**

The reflection and transmission coefficients (*R* and *T*, respectively) can be found using these Fresnel equations for waves polarized parallel to the plane of incidence:

$$\left.\begin{aligned} R &\equiv \frac{I_R}{I_i} = \left(\frac{\bar{\mathscr{E}}_R}{\bar{\mathscr{E}}_i}\right)^2 = \left(\frac{\alpha - \beta}{\alpha + \beta}\right)^2 \\ T &\equiv \frac{I_T}{I_i} = \frac{\varepsilon_2 v_2}{\varepsilon_1 v_1}\left(\frac{\bar{\mathscr{E}}_T}{\bar{\mathscr{E}}_i}\right)^2 \frac{Cos(\theta_T)}{Cos(\theta_i)} = \alpha\beta\left(\frac{2}{\alpha + \beta}\right)^2 \end{aligned}\right\} \qquad \textbf{Equation 26}$$

Section 3.2.2.4 Reflection and Transmission for Perpendicular Polarization

The case of a perpendicularly polarized monochromatic plane wave incident on a boundary, with no charge and no current, between two homogeneous linear media of different optical properties can be solved in much the same way as the case of parallel polarization.

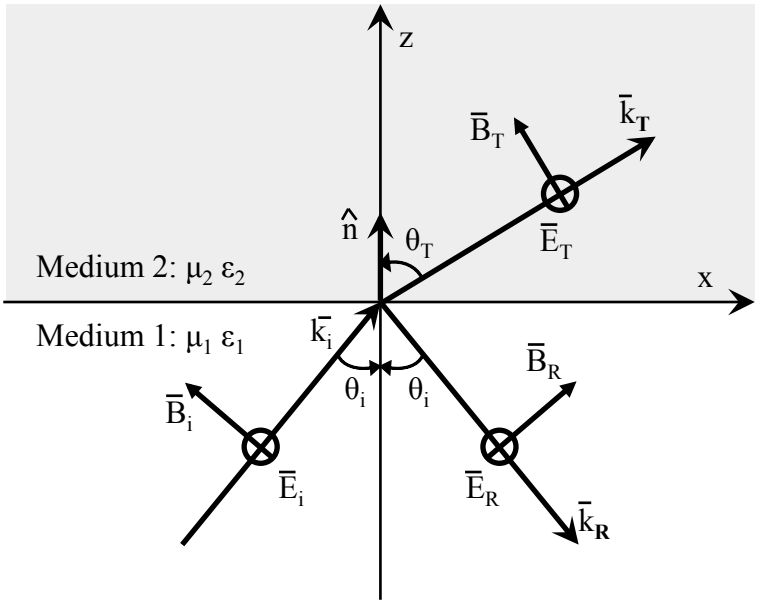

Figure 5: Wave $\bar{k}_i$, with perpendicular polarization, is incident on the plane formed by the $z = 0$ boundary, resulting in reflected wave $\bar{k}_R$ and transmitted wave $\bar{k}_T$.

The reflection and transmission coefficients (*R* and *T*, respectively) can be found using the boundary conditions for waves polarized perpendicularly to the plane of incidence and the geometry defined in Figure 5:

$$\left.\begin{aligned} R \equiv \frac{I_R}{I_i} &= \left(\frac{1-\alpha\beta}{1+\alpha\beta}\right)^2 \\ T \equiv \frac{I_T}{I_i} &= \frac{4\alpha\beta}{(1+\alpha\beta)^2} \end{aligned}\right\} \qquad \textbf{Equation 27}$$

where α and β are defined in Equation 25.

Section 3.3 Experimental Verification of Detecting Fiber Transmission

In the case of a collimated beam, where the polarization transmission coefficients are equal, they are reduced to

$$T = \frac{4n_1 n_2}{(n_1 + n_2)^2}$$ **Equation 28**

The following experiments were done to verify the amount of loss due to reflection. We took measurements, using an optical fiber, of a collimated beam in air and in water. The index of refraction for air and water are known, therefore T can be calculated for each sample type. The ratio of the transmitted powers, P_{Air} or P_{Water}, should be equal to the ratio of the calculated transmission coefficients:

$$\frac{P_{Air}}{P_{Water}} = \frac{T_{Air}}{T_{Water}}$$ **Equation 29**

From experimentation

$$\frac{P_{Air}}{P_{Water}} = 0.91 \pm 0.06$$ **Equation 30**

Using $n_{1air} = 1$ for air, $n_{1water} = 1.33$ for water, and $n_2 = 1.457$ for the fiber core, the transmission ratio is

$$\frac{T_{Air}}{T_{Water}} = 0.97$$ **Equation 31**

As expected, the values in Equation 30 and Equation 31 are equal, within a standard deviation.

A similar experiment was done to verify reflection effects at the sensor. For all experiments, the optical fiber used for detection acted as relay between the beam being measured and a photo detector. There is reflection at the air gap between the fiber and

detector. To verify the extent of this reflection, we directly measured a collimated beam using a sensor in air and in water (though covered with transparent plastic), rather than using an optical fiber relay. In that case, the transmission ratio should be the same as in Equation 30. The ratio of measured power in air and water for this experiment was

$$\frac{P_{Air}}{P_{Water}} = 0.95 \pm 0.02 \qquad \textbf{Equation 32}$$

which is also within a standard deviation of the expected value.

Section 3.4 Optical Fiber Loss Mechanisms

A laser dosimetry device must be capable of determining whether or not a laser therapy device delivers the dose claimed by the manufacturer to the appropriate tissue, above an objectively verified therapeutic dose level and below standardized safety levels. Although the experiments of this thesis do not include an *in-vivo* human trial, the ultimate goal of this area of research is to develop a viable needle/optical fiber based system that is both accurate and minimally invasive. For this reason, an optical fiber was exclusively used in all experiments. However, the power readings obtained via a fiber optic relay experience losses over the length of the fiber. The degree to which the signal is attenuated depends heavily on the fiber material, manufacturing processes, and operation wavelength. The following sections discuss sources of power attenuation.

Section 3.4.1 Material Absorption

Due to electronic and vibrational resonances, all materials exhibit absorption at certain wavelengths. This absorption falls into two categories: intrinsic and extrinsic absorption. Intrinsic absorption is caused by inherent optical fiber material properties and is dependent on wavelength. The optical fiber used (Newport F-MSC) had a 600 μm

diameter pure silica core (SiO_2) and a 630 μm diameter bonded hard polymer cladding. Silica molecules resonate electronically in the ultraviolet range and vibrationally in the infrared range [7]. However, these absorption bands extend into the visible range, as a result of the amorphous nature of fused silica [7].

Extrinsic absorption is caused by impurities present in the fiber. Manufacturing processes and tolerances dictate the concentrations of impurities such as transition-metals (e.g. Fe, Cu, Co, Ni, Mn, Cr), but modern advancements in fiber fabrication techniques have allowed producers to create fibers with metal impurities below 1 part per billion, which can attain a loss level below 1dB/km [7]. However, the presence of water vapor remains the main source of vibrational resonance extrinsic absorption [7].

Section 3.4.2 Scattering

Scattering can be divided into two categories: linear and nonlinear. When light experiences elastic scattering, the amount of energy transferred is linearly proportional to the power of the initial wave and therefore the scattered light retains its initial frequency. This type of scattering is known as linear scattering. Nonlinear scattering of light results in either an upward or downward shift in frequency. However, nonlinear processes generally require much higher intensity electromagnetic fields than need to be considered for this case. Linear scattering within silica optical fibers is generally the result of either Rayleigh or Mie scattering [7].

During fabrication, silica is temporarily molten, allowing its molecules move randomly before it hardens. This movement forms density fluctuations in the fiber core, and consequently fluctuations in the index of refraction. Rayleigh scattering is the term applied to the elastic scattering that occurs due to variations in the refractive index on a

scale smaller than the optical wavelength λ. More specifically, it is when the ratio between the diameter of the scatterer and the wavelength approaches zero [8]. This attenuation factor can be written as

$$\alpha_R = \frac{C}{\lambda^4}$$ **Equation 33**

where C is a constant that is dependent on the material of the fiber core and ranges from 0.7-0.9 dB/km-μm [7]. Attenuation occurs when the light is scattered at an angle that does not allow for continued propagation.

When light interacts with particles that are comparable in size to wavelength, it is more often scattered in the forward (rather than backward) direction. This phenomena is called Mie scattering and is generally due to imperfections such as index of refraction variations or impurities at the core/cladding interface and bubbles in the fiber [9]. Mie scattering is essentially negligible for our purposes.

Section 3.4.3 Attenuation

Attenuations due to the factors discussed in this section are typically rolled into a single attenuation coefficient, α, which is defined as

$$\alpha[dB/km] = -\frac{10}{L}\log_{10}\left(\frac{P_{out}}{P_{in}}\right)$$ **Equation 34**

where L is the length of the fiber, P_{in} is the input power, and P_{out} is the output power. Because all the contributing fundamental loss mechanisms are wavelength dependent, α is also wavelength dependent. The optical fiber used in these experiments was approximately one meter in length. The manufacturer, Newport, lists α to be 0.008 dB/m.

It is likely that macro-bending contributed significantly to observed loss. Macro-bending describes the situation of physical bends in the optical fiber occurring at a radius small enough to sufficiently disrupt the propagating beam angle, causing leakage. The system set-up necessitated bending the fiber to a radius lower than its minimum bend toleration, which is listed as 58 mm by the manufacturer. It is not possible to mathematically calculate attenuation of this form, however there are ways of determining it experimentally. The next section will explain an experiment derived for the purpose of calibrating the dosimetry detection system by determining an effective attenuation coefficient.

Section 3.5 Calibration

The system designed for this project includes an optical fiber (600 um core diameter), which detects the input Gaussian beam profile produced by the laser source. The peak data point for each beam profile measured represents the total power integrated over the area of the fiber core. Figure 6 illustrates that the area over which power is integrated for the peak value of the data collected using an optical fiber cannot be approximated as a single point of the actual beam profile. Figure 7 shows an example of one-dimensional scans produced using the fiber optic detector.

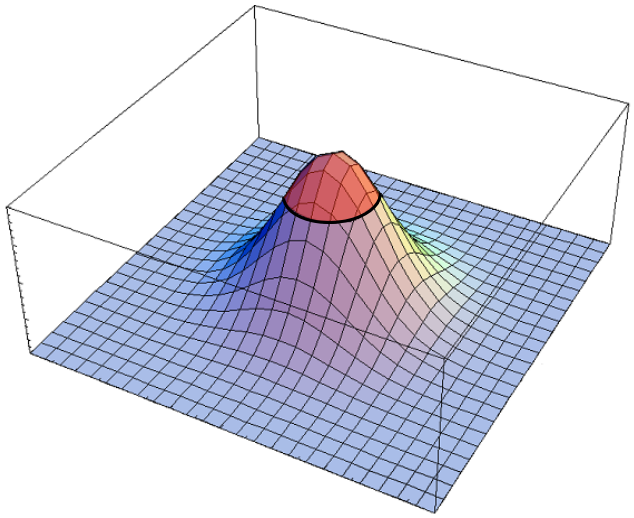

Figure 6: Illustrates the area (in red, circled by a black ring) of a Gaussian beam that is integrated for the peak value measured using an optical fiber.

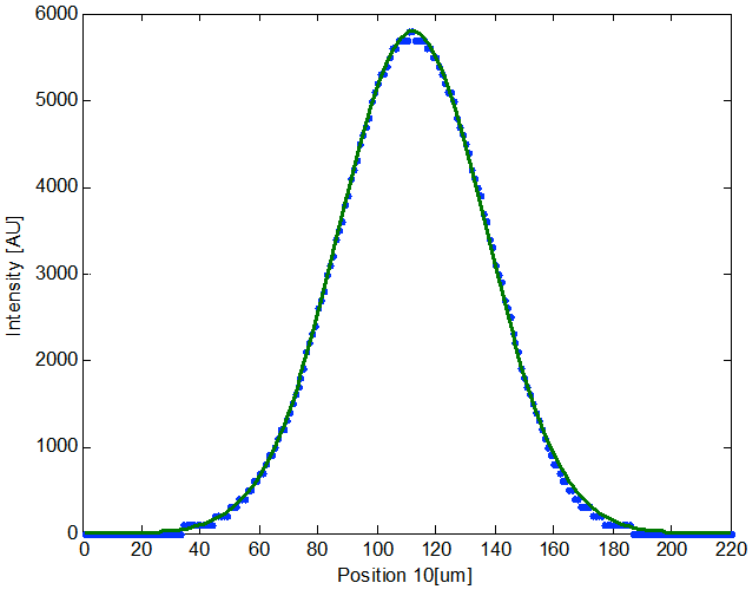

Figure 7: An example of the one-dimensional scans produced using the fiber optic detector (blue points) and the Gaussian curve fitted to the data (green line).

The goals of the calibration are:

- Solve for a correction factor, F, to be applied to all future data sets so that the resultant data can be labeled in absolute values; and
- Verify a method to solve for an appropriate amplitude for each data set Gaussian fit function such that integration over the area of the beam width of the intensity function yields an accurate dose measurement.

The beam width is defined as the beam diameter at the point where the power has fallen to $1/e^2$ of the maximum power.

Section 3.5.1 Solving for Calibration Correction Factor, F

Three types of data were taken to calculate F

1) Optical fiber: beam profiles collected by scanning across the beam center (Figure 8)
2) Total power: single values of total power integrated over the entire beam (Figure 9)
3) Aperture area power: single values of power integrated over defined area (Figure 10)
    a) Aperture #1 - 1254.61 μm diameter
    b) Aperture #2 - 2138 μm diameter
    c) Aperture #5 - 503.91 μm diameter

    Figure 8 illustrates the experimental set-up used in the determination of F. It is shown in the configuration used to take data by computer control, scanning along a straight path across the beam profile using an optical fiber (600 μm core), which yielded 1-dimensional beam profile data sets (data set type 2, listed above). An example of such sets is shown in Figure 7. Alternately, the optical fiber was replaced by a photodetector (Newport model 818-ST) covered in a thin plastic

covering (data set type 1, listed above). This configuration, which is illustrated in Figure 9, allowed for the use of the entire detector area (1 cm^2) without the attenuation loss of an optical fiber relay. The third data set type used in this calculation resulted from beam peak measurements taken while the photodetector was covered by cases with a variety of apertures (illustrated in Figure 10).

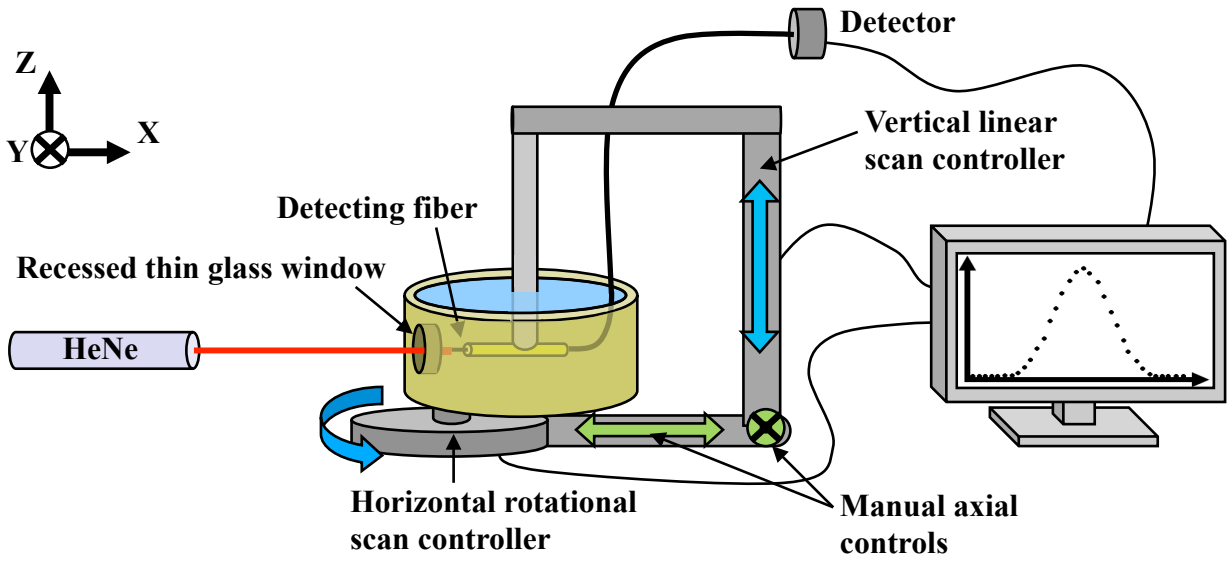

Figure 8: The experimental set-up used to calibrate the system. The source was a HeNe laser (Melles Groit, max power measured was 26.7mW at 632.8nm, before the thin glass window). The beam passed through a thin glass window (Fisherbrand microscope cover glass 0.13-0.17mm thick) which was recessed. Lenses were placed in the window recession for divergent beam measurements. The detecting fiber (Newport F-MSC, step index, 600um core, 0.37 NA) was attached to computer controlled actuators (Newport 850G) and manually controlled micrometers. The beam profile was scanned linearly in the z direction and rotationally about the z-axis. Manual controls were used to adjust the depth within the liquid phantom and to locate the beam peak position. The system was manually controllable in x, y, and z directions.

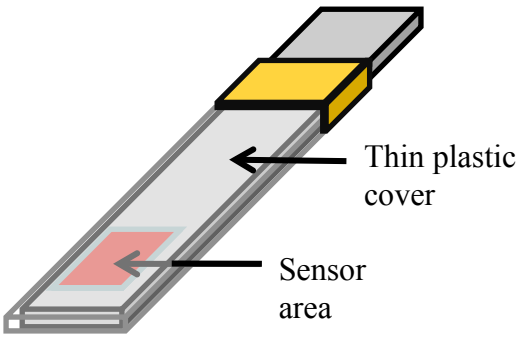

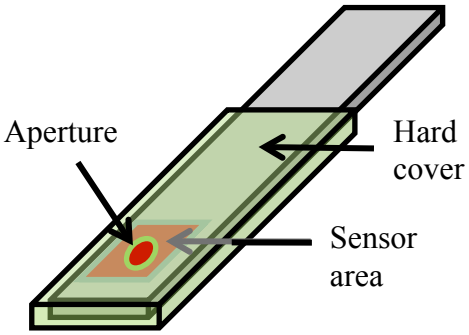

Figure 9: Photodetector covered by a thin clear plastic cover, used for obtaining data set type 2.

Figure 10: Photodetector covered by an opaque casing with various apertures, used for obtaining data set type 3.

First, we took several linear scans of a collimated beam's profile and fitted a Gaussian curve to each data set. From those fitted curves the following values were obtained by averaging over all of the scanned data sets: maximum value, in mW, σ, and beam width, in μm. The Gaussian curve is centered on 0 (to ease later integration). It assumes that the attenuation in the detection fiber decreased all signals linearly. The system configuration used to measure beam profiles utilized a different photodetector than the one used for total power or aperture power (data types 2 and 3, respectively). It is assumed that the difference between each photodetector is linear, therefore the correction factor F can include the factor which relates the photodetectors and can account for attenuation. The power measurement (type 2) take over the entire area of the beam profile is assumed to need no correction factor (for the purpose of solving for F), but it also has no beam profile structure information.

The goal of this calibration is to obtain an intensity function, $Fn_{dose}[x]$, which can be used to integrate mathematically over the range dictated by beam width to calculate a dose. The form of this Gaussian equation, for this particular case (a collimated beam of 1 mm width in air), is as follows:

$$G[x] = A \cdot e^{\frac{-x^2}{2\sigma^2}}, \qquad \textbf{Equation 35}$$

where the amplitude A is unknown and the standard deviation σ was derived from the beam profile data (type 1). The integration of this function from 0 to infinity and rotated 2π about the vertical axis gives the function

$$A_{tot} = 2 \cdot A \cdot \pi \cdot \sigma^2, \qquad \textbf{Equation 36}$$

where A_{tot} is the total power measurement found by using the entire detector surface (type 2). Equation 36 was used to solve for an amplitude, A, associated with a particular σ.

The product of the correction factor, F, and the peak value, A_{fiber}, of the optical fiber beam profiles measurements (type 1), is assumed equal to the intensity function found using Equations 35 and 36 integrated over the radius of the fiber core, r_{core}:

$$A_{fiber} \cdot F = 2\pi \int_0^{r_{core}} x \frac{A_{tot}}{2\pi\sigma^2} e^{\frac{-x^2}{2\sigma^2}} dx. \qquad \textbf{Equation 37}$$

Equation 37 was used to determine a universal correction factor F for this optical fiber based detection system. $Fn_{dose}[x]$ must be determined for each phantom or tissue sample and/or source.

Section 3.5.2 Verifying the Intensity Function

$Fn_{dose}[x]$ for the experimental parameters specified for system calibration is

$$Fn_{dose}[x] = \frac{A_{tot}}{2\pi\sigma^2} e^{\frac{-x^2}{2\sigma^2}}, \qquad \textbf{Equation 38}$$

where A_{tot} and σ are as defined in the previous section. To verify the accuracy of this function, several measurements were taken using the configuration that incorporates

opaque photodetector covers with various apertures (type 3). Each aperture represents a power integration of the beam profile over the area of the aperture. $Fn_{dose}[x]$ was integrated over the area of each aperture to calculate theoretical power measurements, which were then compared to the actual power measurements obtained using the apertures.

Aperture	*Radius [um]*	*Calc. Power [mW]*	*Measured Power [mW]*	*% Difference*
#2	1069	22.18	21.95	1.01%
#1	627.3	21.23	20.28	4.67%
#5	251.9	8.94	8.76	0.88%

Table 1: Comparison of calculated and measured power values over the area of various apertures.

To calculate the dose for this configuration:

$$Dose[J/cm^2] = \frac{Power[W]}{Area[cm^2]} \cdot ExposureTime[s] \qquad \textbf{Equation 39}$$

$$= 2.467\left[\frac{W}{cm^2}\right] \cdot ExposureTime[s]$$

where the Area was defined by the beam width and the power was determined by integrating $Fn_{dose}[x]$ over the area represented by the measured beam width. This verifies that an optical fiber based system can be accurately and precisely calibrated. A single calibration per fiber used is required for the calculation of the factor F. A calibration per data set is required to find (1) the term σ appropriate for the function $Fn_{dose}[x]$, the integration of which yields the power measurement for the dose calculation, Equation 39

and (2) the area encompassed by the beam width, which is also used in the calculation of dose.

CHAPTER 4 CONSIDERATIONS FOR SCAN PATH: LINEAR VS ROTATIONAL

Section 4.1 Introduction

All proposed experiments utilize optical fibers for light detection. The acceptance angle, associated with the numerical aperture (NA) of a fiber, limits the fiber's effective detection range depending on the angle at which scattered light is incident upon the detecting surface of the fiber. The focus of this chapter is experimentation, motivated by NA system limitations, to determine the optimal orientation of the detection fiber with respect to the scattered light being measured and to determine how the shape of the fiber scan path maintains said orientation. In Section 4.1.1, we discuss why this is a necessary consideration for future experimentation. Later sections will propose two different methods for detection orientation (called linear and rotational) and detail how these methods were modeled, tested and compared.

Section 4.1.1 Motivation

Proposed experiments include the study of beam propagation through liquid fat emulsions with optical properties similar to human tissues, and thin biological tissue slices. These experiments will study the structurally-induced scattering effects of various tissue types and tissue layer combinations on the dose of laser therapy devices as the beam propagates through the sample. Please note that the aforementioned future experiments had not yet been conducted, as of the writing of this thesis, and are not the focus of it.

Optical fiber will be used for detection in future experiments (and was used in the experiments described in this thesis) so that the laser wavelength can be varied without changing the system alignment, allowing measurements of the same sample to be taken at exactly the same position for all wavelengths. Using an optical fiber also provides the benefits of a defined aperture, which has a smaller diameter than that of the beam profile to be measured, and a small cross-sectional profile without overhanging obstructions. These attributes allow for the derivation of a single calibration, which renders measurements in absolute values usable across various experiments (discussed in Chapter 3) to determine laser dose.

Using an optical fiber, rather than an encased detector, allows the detecting surface to be in contact with the sample without interference from a sensor casing or cover. The motion and scan distance range of the detection fiber would be limited by the physical constraints of the experimental system. These limitations will be further discussed in this chapter along with the experiments done to determine their extent. Optical fibers are also limited in their detection range by the acceptance angle defined by their numerical aperture. The same fiber should be used for all proposed experiments regardless of whether measurements are taken in air or liquid for the sake of limiting variables between comparable data sets.

In future experiments, tissue samples and liquid tissue phantoms will be prepared so that the scattered beam's initial Gaussian profile will remain measureable at all data sampling positions. The Gaussian beam profile will be scanned using optical fiber to measure the dose of the laser beam at various depths in the tissue sample/phantom. In the

completed experiments Gaussian beam profiles were also measured for the purpose of comparing the achievable accuracy possible using different detection fiber scan paths.

Two scan path shapes are proposed for future experiments: linear and rotational. These scan paths are illustrated in Figure 11 (linear) and Figure 12 (rotational). Each figure shows an initial laser beam incident upon a thin slice of tissue that scatters the beam. At positions #1 and #2, beam profile scans a_1 and a_2 are taken. For linear scans, this one-dimensional data set is taken as the fiber is moved along the z-axis, while keeping the detection surface parallel to the z-y plane. This orientation allows measurements to be taken at increments along the z-axis. However, this optical fiber orientation is limited in its light acceptance angle capability for largely scattered beams by the fiber's NA. For this reason, a rotational scan path was proposed. As illustrated in Figure 12, the rotational scan path moves the optical fiber along a circular curve, rather than a straight line. This curve is centered on the position at which the beam is incident upon the tissue sample. Again the optical fiber detection surface is oriented parallel to the z-y plane; however, in this case the y-axis is circularly curved. By following this path, the angle of light incident on the fiber is kept well below the threshold of limitation dictated by the NA.

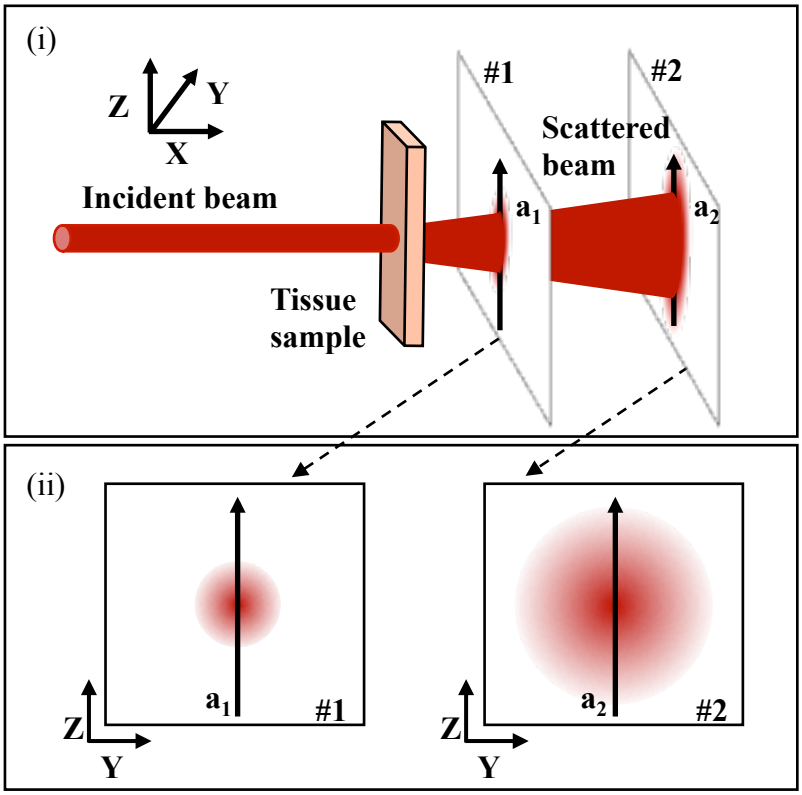

Figure 11: Proposed linear scanning method for imaging the profile of a laser beam scattered through a tissue sample. Scans a_1 and a_2 are one-dimensional scans taken across the beam at positions #1 and #2 respectively. At least two scans at various positions along the direction of propagation (x-axis) are required to determine the dose of radiation at a depth within the tissue equal to the thickness of the sample by enabling measurements of beam width, and subsequently beam divergence angle. The divergence angle would be used to determine the beam width, and therefore dose, at the desired position.

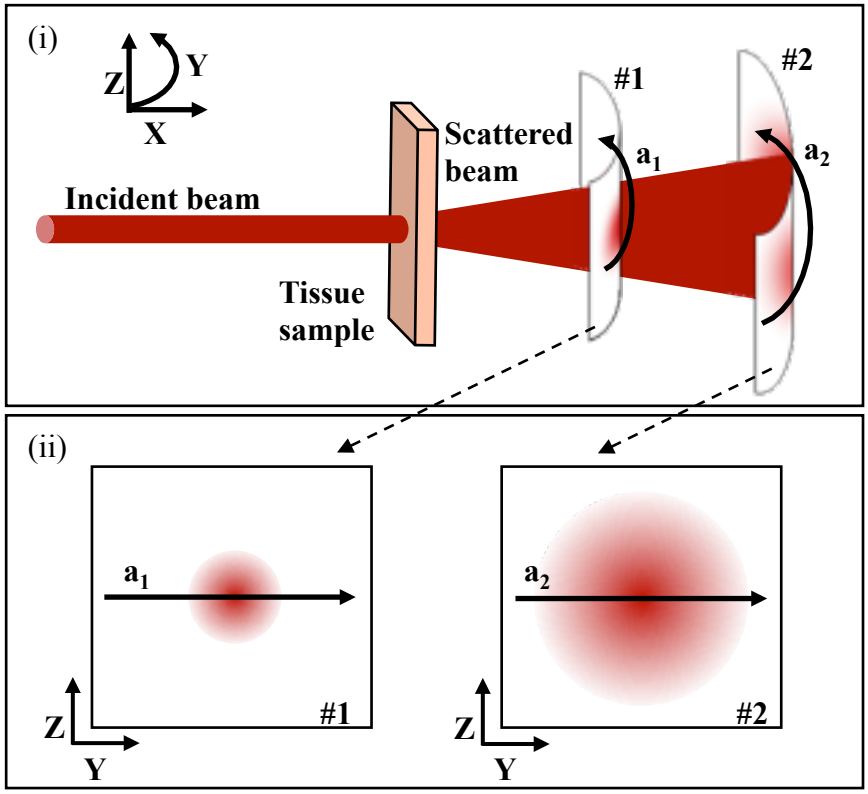

Figure 12: Proposed rotational scanning method for imaging the profile of a laser beam scattered through a tissue sample. Scans a_1 and a_2 are one-dimensional scans taken across the beam at positions #1 and #2 respectively. At least two scans at various positions along the direction of propagation (x-axis) are required to determine the dose of radiation at a depth within the tissue equal to the thickness of the sample by enabling measurements of beam width, and subsequently beam divergence angle. The divergence angle would be used to determine the beam width, and therefore dose, at the desired position.

Before these proposed experiments can be completed the system limitation (imposed by range of motion, scan path, or NA) must be determined. Testing and understanding such limitations will allow us to develop a reliable testing apparatus and procedure for the study of laser propagation through tissue and future therapeutic laser device safety and efficacy verification.

Section 4.1.2 Goals

In this chapter we discuss experiments we completed for the purpose of testing the limitations and accuracy of the scanning system and proposed scan paths. The scanning system set-up is illustrated in Figure 13. The proposed scan paths were introduced in Section 4.1.1 and illustrated in Figure 11 (linear scan path) and Figure 12 (rotational scan path) as proposed for future experiments involving tissue samples.

Regardless of scan path, physical constraints of the testing apparatus and the fiber itself limit the detection fiber motion. A goal of the experiment was to determine the extent that physical limitations impaired the system's ability to measure scattered beams. In particular, we determined at what divergence angle a beam profile becomes unmeasurable.

Another goal of this experiment was to determine the optimal scan path. The linear scan path moved the detection fiber in a straight line, such that the perpendicular orientation of the fiber's detecting surface with respect to the beam's direction of propagation was maintained. The rotational scan path moved the detection fiber in a circular arc centered around the plane upon which the beam initially entered the sample. Both scan paths crossed the beam at its center and allowed measurements to be taken of the beam profile.

Linear scanning offered a simple solution, because its straight path allowed a straightforward determination of divergence angle. However, the NA of the detection fiber limited these measurements and it was hypothesized that the measured divergence angle using linear scan data would converge to a particular angle, dictated by the fiber's NA, as the input beam divergence angle was increased. It was a goal of this experiment to

determine which factor imposed the greatest limitation to linear scanning: the NA of the fiber or physical range of motion limitations (the sample vat size and allowable fiber bend radius).

Rotational scanning was appealing because it was free from NA limitations. However, the measurements were taken along a curved path and therefore required a conversion calculation to determine the divergence angle of the scattered beam. It was a goal of this experiment to determine if the benefits of the rotational scan path outweighed the possible errors introduced by the conversion.

To determine the optimal scan path, several beams with progressively larger divergence angles were scanned using both scan paths. The beams were scattered using lens to maintain profile uniformity. The resulting divergence angles measured using each path type were compared against theoretically calculated beam divergence angles for each scattered beam. Each scan type was also examined to determine which of the aforementioned scanning limitations were the most detrimental to measurement accuracy.

In Section 4.2, the testing apparatus and the procedures used for experimentation are described. This includes a detailed discussion of each tested scan path.

In Section 4.3, theoretical divergence angles provided by each of several lenses used in experimentation are derived. These lenses were used for the purpose of modeling light scattered through tissue. The experimentally determined divergence angles were compared to those calculated theoretically to determine which scan path yielded the most accurate results. Measurements were taken for various lenses until the beam was scattered beyond the physical detection range of the system. The angle at which this

occurred was determined based on the theoretical calculations and is discussed in this section.

In Section 4.4, we derive a theoretical model of the divergence angle expected to result from measurements taken via the linear scan path. This was done by first calculating a function that represents the limitation imposed on the detection fiber's incident angle acceptance window, which is dependent on the input beam divergence angle (calculated in Section 4.3), and the position of the fiber along the axis of beam propagation. This function was then used to alter an ideal model of a Gaussian beam to produce a model beam profile for expected linear data measurements. We calculated expected divergence angles from the modeled beam profiles. By plotting the modeled against the input divergence angles we determined the angle to which linear scan angle measurements would theoretically converge as the input divergence angle increased. The hypothesized convergence was used in the assessment of the accuracy yielded using a linear scan path.

In Section 4.5 we derive a conversion factor for beam profile measurements taken using a rotational scan path. The procedure for determining divergence angle via this scan path included taking power readings along a circular arc; the position of each such reading was recorded in units of angle rather than distance. To properly determine divergence angle, and to ensure accurate side-by-side comparison to linearly scanned data, the position measurements were required to be converted to units of distance.

In Section 4.6 we derive an equation used to determine divergence angle from experimental data, taken along either scan paths.

In Section 4.7 we present and discuss experimental results and compare measurements resulting from each scan path data set to theoretically determined divergence angles for the purpose of establishing the optimal scan path for testing the dose of laser therapy devices. The model of expected linear scan data is also compared to experimental results to assess the extent of limitations imposed by the fiber NA.

Section 4.2 Experimental Set-up

The experimental set-up is illustrated in Figure 13. The source was a Melles Griot helium-neon (He-Ne) laser, which emitted at 632.8nm at a measured total maximum power of 26.7 mW. This collimated beam was directed through a lens and a thin glass window (1 mm thick) into the detection vat. Objective lenses, of various magnification powers, were placed in the beam path for successive experiments to create scattered beams of uniform distribution, but with varying divergence angles. These lenses will be discussed in greater detail in Section 4.3. The thin glass window, Fisher microscope cover glass 12-542-B measuring 22mm × 22mm × 1mm, was sealed to the detection vat in a recess. The recess was placed so that the side of the glass window closest to the detection fiber was positioned approximately at the rotational point of the horizontal rotational scanner. The detecting fiber (Newport F-MSC, step index, 600um core, 0.37 NA) was positioned in the vat, which in other experiments would be filled with a sample liquid. The vat was also equipped with a sample holding stage, which directly abutted the glass window. The scans were taken in air, but within the confines of the vat to add continuity across experiments and as a proof-of-concept that measurements can be taken

by a large core diameter fiber within a vat without exceeding the fiber's maximum bend radius limit.

Detecting fiber motion was controlled on the x and z-axes by computerized Newport 850G actuators. The x-axis position was selected and entered for each data measurement set. A Newport SDS65 linear stage was used to control the y-axis, which was set manually to center the detector on the scattered beam. Linear scan measurements were taken by moving the detecting fiber in the z-direction using the vertical computerized actuator. Rotational scan measurements were taken by moving the detection fiber in the x-y plane using a Newport UR8755C actuator and UE34CC motor.

For linear scans, the detector was an Ophir 3A power/energy detector (P/N1Z02621) attached to an Ophir Nova II power/energy meter (P/N 1Z01550). For rotational scans the detector was a Newport 818-ST silicon photodetector attached to a Newport 841-PE power/energy meter. Each set of detectors and scanning actuators (one for linear scans and one for rotational scans) was attached to a computer equipped with an actuator motion controller/driver and a LabVIEW program capable of taking power and position measurements while moving the detection fiber across the beam profile along either scan path.

Two separate computer systems were required for the two different scan paths due to actuator controller/driver limitations. As a result, two different sensors were used for photo-detection. For the experiment discussed in this chapter, beam profile measurements were taken to determine beam width and divergence angle, these being spatial measurements, the absolute power values were irrelevant and therefore only given in terms of arbitrary units (AU). For experiments that necessitated an absolute power

measurement, calibrations were done which encompassed the difference between power meters, as well as reflection and attenuation in the fiber. These calibrations are derived/discussed in Chapter 3.

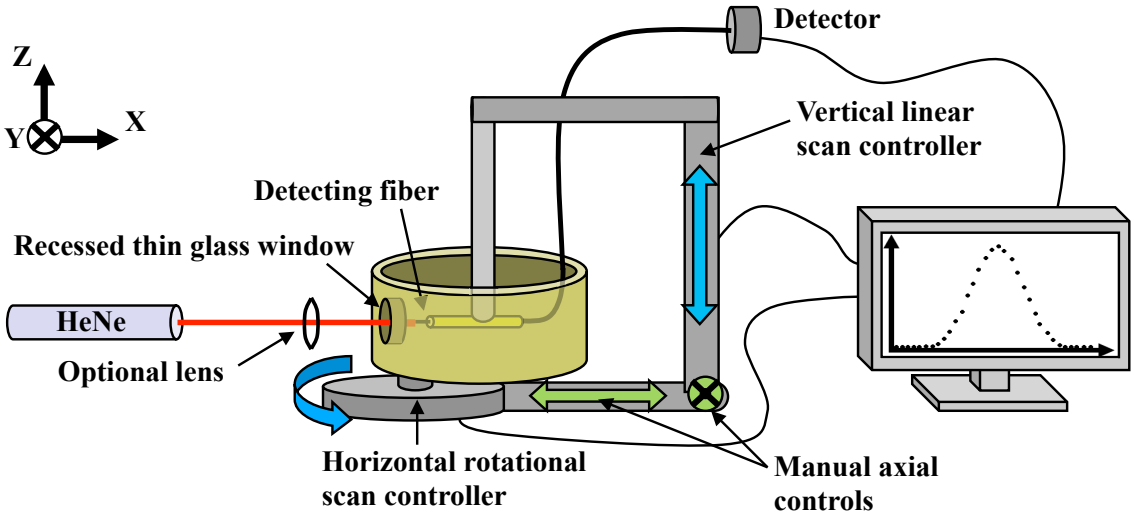

Figure 13: Experimental set-up. The source was a Melles Griot helium-neon (HeNe) laser that emitted at 632.8nm at a measured total maximum power of 26.7mW. This collimated beam was directed through a lens and a thin glass window (1 mm thick) into the detection vat. The detecting fiber was set in the vat. Detecting fiber motion was controlled on the x and z-axes by computerized Newport 850G actuators. The x-axis position was selected and entered for each data measurement set. A Newport SDS65 linear stage was used to control the y-axis, which was set manually to center the detector on the scattered beam. Linear scan measurements were taken by moving the detecting fiber in the z-direction using the vertical computerized actuator. Rotational scan measurements were taken by moving the detection fiber in the x-y plane using a Newport UR8755C actuator and UE34CC motor. For linear scans, the detector was an Ophir 3A power/energy detector (P/N1Z02621) attached to an Ophir Nova II power/energy meter (P/N 1Z01550). For rotational scans the detector was a Newport 818-ST silicon photodetector attached to a Newport 841-PE power/energy meter. Each set of detectors and scanning actuators (one for linear scans and one for rotational scans) was attached to a computer equipped with an actuator motion controller/driver and a LabVIEW program capable of taking power measurements while moving the detection fiber across the beam profile.

Section 4.2.1 Scan Paths

Two scan paths were tested and compared: linear and rotational. Figure 14 and Figure 15 illustrate the difference between the two paths and show the basic set-up for the completed experiments. When a laser beam is incident upon a tissue sample it is scattered, though not in a perfectly uniform way. Lenses were used to model tissue sample light scattering in the experiment to compare the accuracy of scan paths.

Linear scans were taken by moving the detecting fiber in a straight path across the beam profile in a line perpendicular to the direction of beam propagation, which maintained a fiber detection surface orientation perpendicular to the direction of beam propagation.

Rotational scans were taken by moving the fiber in a circular arc across the beam profile, which allowed the fiber detection surface to always be orientated such that the angle of light incident on the fiber would remain significantly smaller than the limiting acceptance angle dictated by the fiber NA.

It was particularly important that the scattered beam be uniformly distributed so that the beam profile could be taken at any cross-section that passed through the beam center. To ensure that the measurements taken along both scan paths were taken at the same position on the axis of beam propagation, the detection fiber had to be attached to the scanning controllers for both scan paths simultaneously. The scanning hardware was arranged so that the center positions for both scan paths were exactly the same. This position also coincided with the center of the scattered beam to ensure that imaged beam profiles accurately represented the beam. It was not physically possible to set the actuators to scan both paths along the same plane. As discussed in Section 4.2, the linear scan path actuators moved the detection fiber along the z-axis (defined in the system set-up illustration, Figure 13) and the rotational scan path actuators moved the detection fiber along an arc in the x-y plane (also defined in Figure 13). The radial scattering uniformity provided by the lenses and the co-registered center position of the scan paths allowed the measurements taken via each scan path to be comparable.

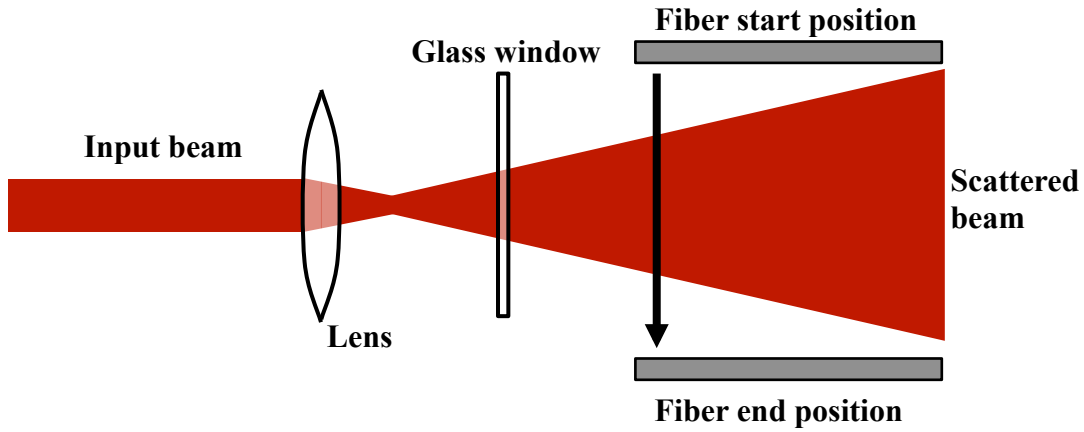

Figure 14: Linear Scanning Path. The path of the detection fiber is shown with an arrow, which correlates to z-axis shown in Figure 13.

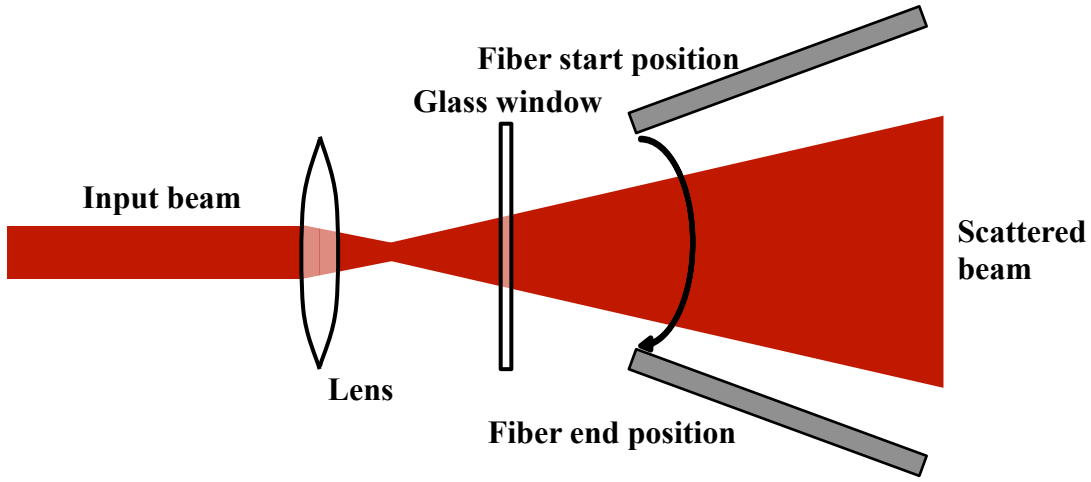

Figure 15: Rotational Scanning Path. The path of the detection fiber is shown with an arrow, which correlates to an arc in the x-y plane shown in Figure 13.

Section 4.2.2 Data Collection Process

Figures 16 and 17 illustrate the data collection process for each scan path. Neither Figure shows the detection fiber. The arrows labeled a_1 and a_2 depict the motion of the detection fiber, the detection surface of which was oriented parallel to the y-z plane in both figures. Note that the y-axis in Figure 17 is circularly curved and therefore the path taken by the fiber includes a simultaneous rotation about the z-axis to maintain the detection surface orientation in relation to the curved y-z plane. In both figures part (i)

shows the experimental set-up, including the glass window of the sample vat, part (ii) shows the axis along which each scan, a_1 or a_2, is taken with respect to beam profile at x-position #1 and #2, respectively, and part (iii) shows a representation of the data taken along scan lines a_1 and a_2.

First, the detection fiber was positioned so that it was in contact with the glass window. All x-positions (along the beam principle vector) were measured with respect to the surface of the glass window, which served as the zero-position. Starting from the zero-position, the x-position for the first measurement was selected and manually entered via the computer-controlled actuator. This position movement corresponds to the arrow labeled c in both figures, and was generally on the order of 1 mm per increment.

Next, the y-position of the detecting fiber was manually centered on the scattered beam using the linear translation stage by maximizing the power level reading. In Figure 16, for linear scans, y-position adjustment corresponds to the arrow labeled b. After finding the center of the scattered beam, the position of the detection fiber was moved in the negative z-direction, away from the beam center, to a position outside of the scattered beam so that a single scan would cover the entire beam width. Linear scans were driven automatically, stopping at intervals along the linear path (a_1) to record a power measurement from the detector. The spatial position was recorded in units of distance (usually nm) and power readings were recorded in AU.

The z-position of the fiber was again centered on the scattered beam before collecting data along the rotational scan path to maintain comparability between scan types. The z-position adjustment corresponds to the arrow labeled b, in Figure 17. For rotational scans, as for linear scans, the y-position could be adjusted using the linear

translation stage, but the center of the rotational scan was further adjusted by manual input to the rotational scanning actuator, along the scan path a_1, which was guided by observed power readings.

After the fiber was positioned on the center of the beam, the rotation scan was performed. The position of the detection fiber was moved using the rotational actuator to a position outside of the scattered beam so that a single scan would cover the entire beam width. Rotational scans were driven automatically and stopped at intervals along the a_1 arrow, shown in Figure 17, to record a power measurement from the detector. The spatial position was recorded in units of angle and power readings were recorded in AU. To be able to compare linear scans to rotational scans, rotational scan spatial positions were converted from units of angle to those of distance. This conversion will be discussed and derived in Section 4.5.

Several linear and rotational scans were taken at each x-position. After completing these scans, a new x-position was set for the next set of linear and rotational scans and adjustments were made as necessary to ensure that the next set of scans, labeled a_2 in Figure 16 and 17, was centered on the scattered beam. Although linear and rotational scans were taken across different axes of the scattered beam, the beam was aligned to be rotationally symmetric. At every x-position interval adjustments were limited to those that would not decouple the spatial correlation between the linear and rotational scans. Care was also taken to preserve the distance between the rotational axis of the rotational scans and the glass window, so that a single calibration could be applied to all rotational data sets.

Beam widths were measured using the scan sets at all x-axis positions. Beam divergence angles were found using those beam widths. Several lenses were used to scatter the collimated laser beam into a symmetrically divergent beam: Newport M-5X, M-10X, M-20X, and M-40X; Edmund DIN60; and Olympus DPlan100. For each lens, sets of linear and rotational data were taken at several x-axis positions and were then used to determine the beam divergence angle. To determine which scan type yielded more accurate measurements, measured beam divergence angles were compared to theoretically calculated divergence angles for each lens/data set.

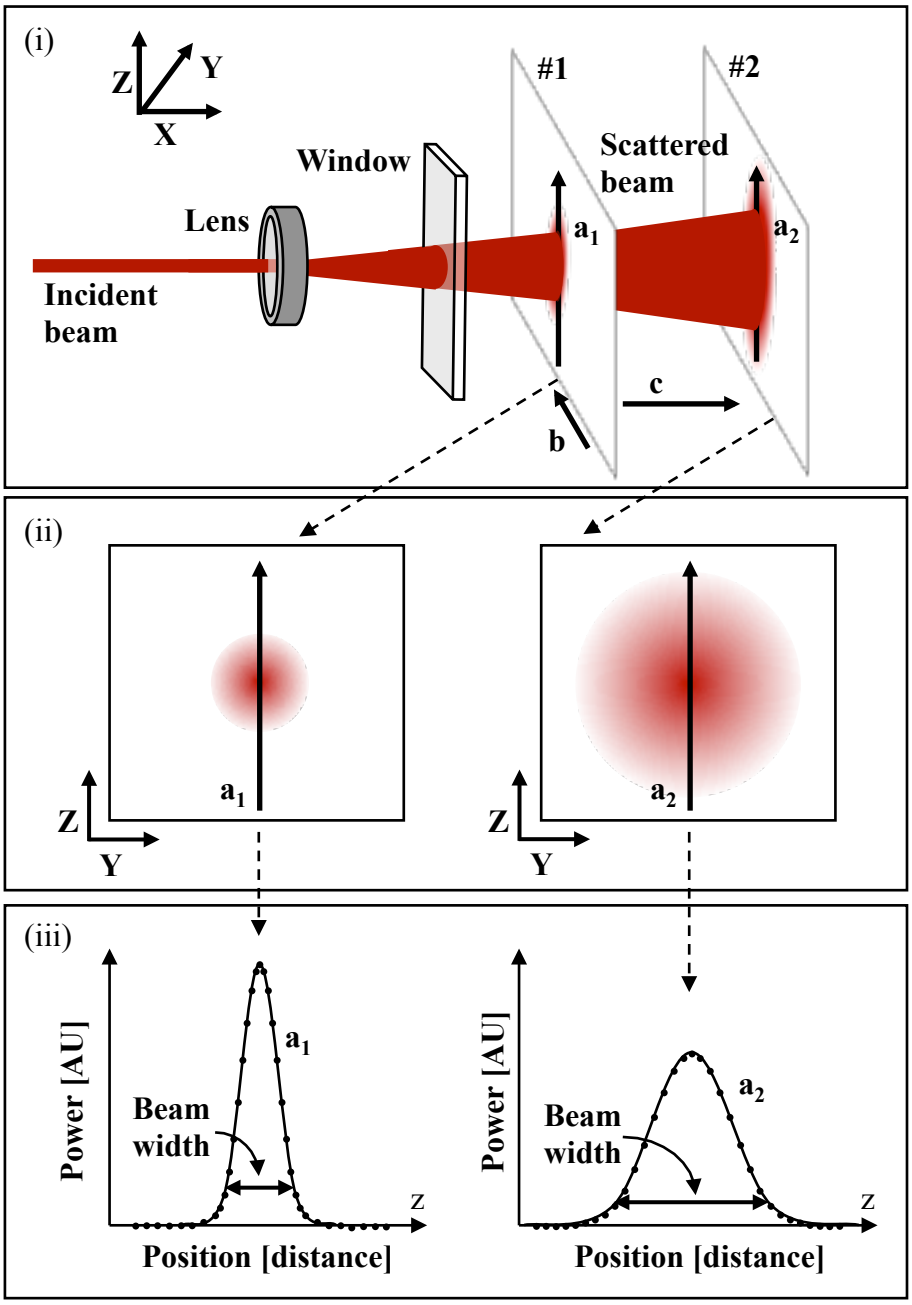

Figure 16: Linear scanning data collection process. (i) shows the experimental set-up, including the glass window of the sample vat, (ii) shows the axis along which each scan, a_1 or a_2, was taken with respect to beam profile at x-positions #1 and #2, and (iii) shows a representation of the data taken along scan lines a_1 and a_2. The detection fiber was set at an x-position (c arrow). The y-position (b arrow) was set manually to center the detection fiber on the scattered beam. Linear scans were automatically taken at intervals along the z-axis (a arrows). At least two scan sets (#1 and #2), from different x-positions (c arrow) were needed to calculate beam divergence.

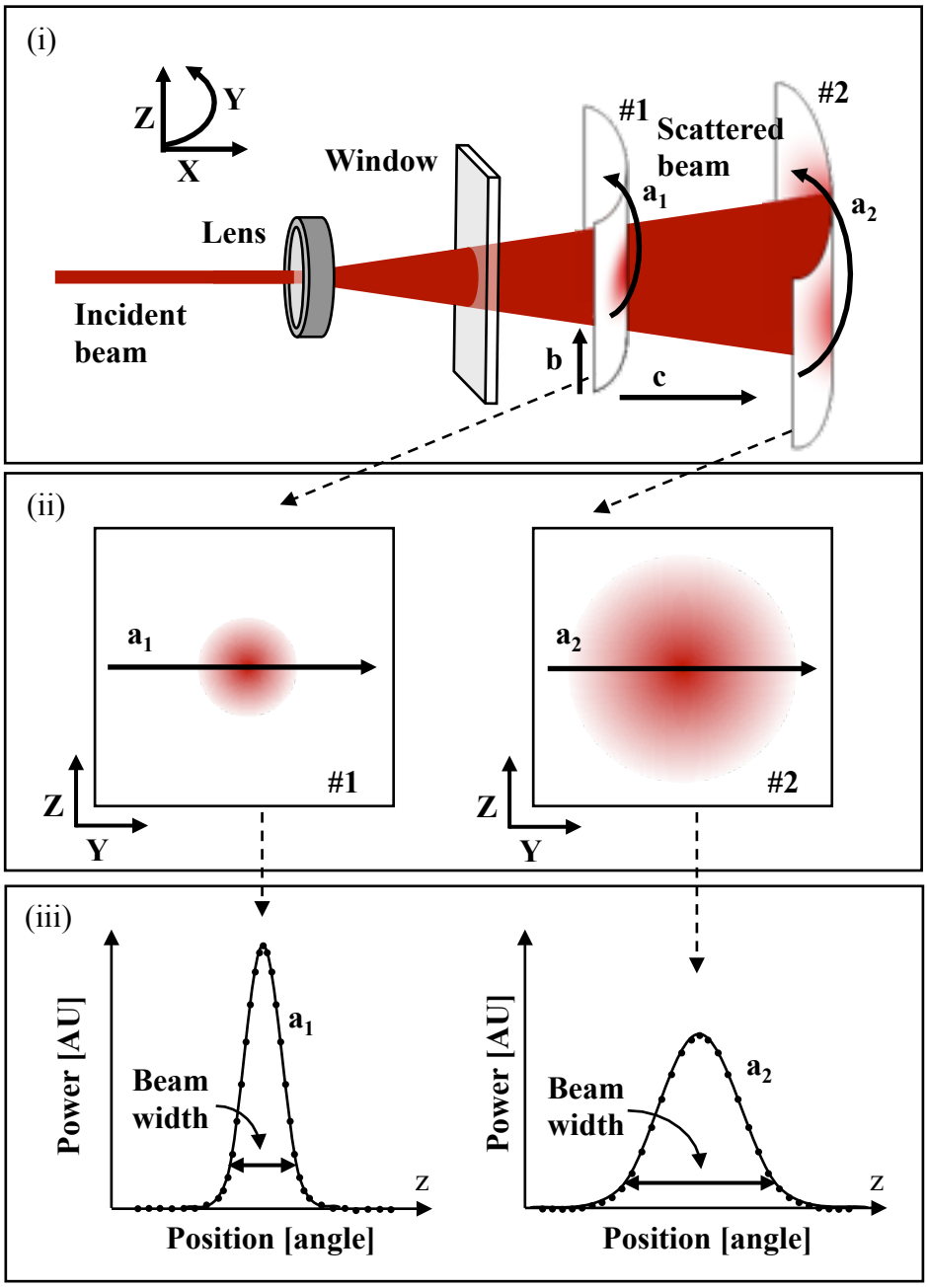

Figure 17: Rotational scanning data collection process. (i) shows the experimental set-up, including the glass window of the sample vat, (ii) shows the axis along which each scan, a_1 or a_2, was taken with respect to beam profile at x-positions #1 and #2, and (iii) shows a representation of the data taken along scan lines a_1 and a_2. The detection fiber was set at an x-position (c arrow). The y-position (a arrow) was set manually to center the detection fiber on the scattered beam. Linear scans were automatically taken at intervals along the y-axis (a arrows). At least two scan sets (#1 and #2), from different x-axis positions (c arrow) were needed to calculate beam divergence.

Section 4.3 Theoretical Divergence Angle Derivation

Several lenses were used as the objective lens, illustrated in the experimental set-up Figure 13, to scatter the collimated laser beam into a symmetrically divergent beam: Newport M-5X, M-10X, M-20X, and M-40X; Edmund DIN60; and Olympus DPlan100. For each of these lenses we calculated an input divergence angle, which was used to assess the accuracy of divergence angle measurements made using linear and rotational scan path data.

Section 4.3.1 Gaussian Beam Parameter Functions Derivation

A Gaussian beam and the parameters associated with the calculation of divergence angle are shown in Figure 18. The beam is propagating along the z-axis, and the point $z = 0$, is located at the beam waist, w_0, which is the minimum width of the beam, wherein beam width is measured at the point at which the power amplitude has fallen to $1/e^2$ of its peak value. The Rayleigh range, z_0, is the distance along the direction of propagation away from the beam waist beyond which the beam divergence becomes linear. The Rayleigh range is defined as

$$z_0 = \frac{n\pi w_0^2}{\lambda}, \qquad \textbf{Equation 40}$$

where n is the index of refraction of the propagation medium and λ is the wavelength of the beam. It is necessary to verify that measurements were taken at a position outside of the Rayleigh range to determine the validity of the geometrically determined divergence angles for each data set.

The divergence angle at any given point along the beam, $\theta(z)$, converges to a single value outside of the Rayleigh range ($z > z_0$) to

$$\theta(z) = \lim_{z\to\infty} \frac{2w(z)}{z} = \frac{2\lambda}{\pi w_0}, \qquad \textbf{Equation 41}$$

where $w(z)$ is the beam width at a given z-position. $\theta(z)$ represents the full angle, at a given location z, over which the beam reduces to half of its maximum intensity at the center of the beam. The properties of a Gaussian beam can be completely predicted if the beam waist and radius of curvature are known at any one z-position. The beam width is defined as

$$w(z) = w_0\left[1 + \left(\frac{\lambda z}{n\pi w_0^2}\right)^2\right]^{1/2}. \qquad \textbf{Equation 42}$$

The beam wavefront curvature of a Gaussian beam located at a distance z from the beam waist is

$$R(z) = z\left[1 + \left(\frac{\pi w_0^2}{\lambda z}\right)^2\right]. \qquad \textbf{Equation 43}$$

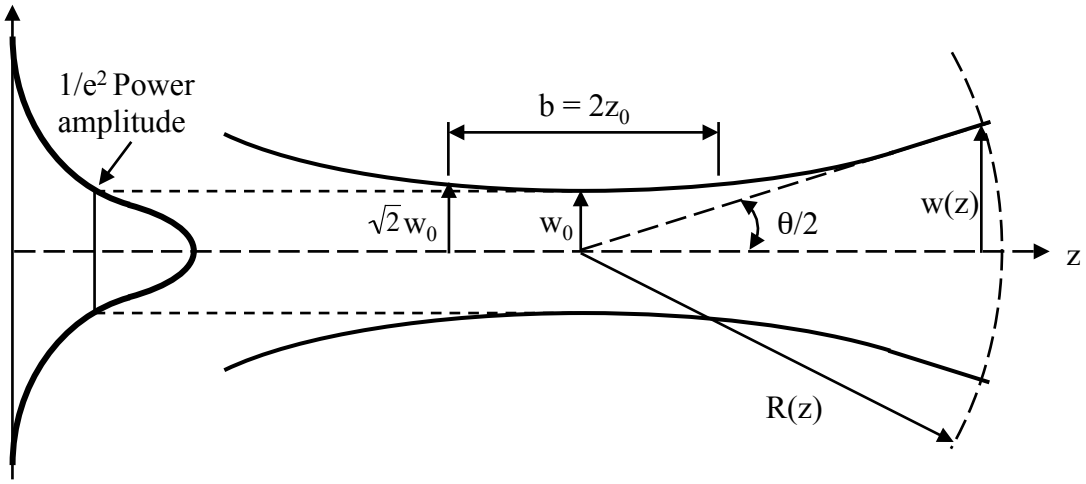

Figure 18: Gaussian beam parameters associated with angular divergence derivation: beam waist w_0 at $1/e^2$ of the power amplitude, distance from beam waist z, Rayleigh range z_0, confocal parameter b, beam width at distance z, $w(z)$, radius of curvature at distance z, $R(z)$, and divergence angle θ.

The calculation of the divergence angle of a beam that has passed through a lens involves the use of ABCD matrices. This technique consists of performing transformation on the complex beam parameter of a Gaussian beam, q, which is defined as

$$\frac{1}{q} = \frac{1}{R(z)} - j\frac{\lambda}{n\pi w^2(z)}, \qquad \textbf{Equation 44}$$

where $j = \sqrt{-1}$. The parameter, q, includes beam information at location z. The complex beam parameter at one location, q_1, can be used to calculate beam parameters at another location, q_2, using the ABCD matrix

$$q_2 = \frac{Aq_1 + B}{Cq_1 + D}, \qquad \textbf{Equation 45}$$

where the values of A, B, C and D are determined by transformation parameters. To more easily use Equation 44, Equation 45 can be rewritten as

$$\frac{1}{q_2} = \frac{C + D(1/q_1)}{A + B(1/q_1)}. \qquad \textbf{Equation 46}$$

Using the form of Equation 44, Equation 46 can be written as

$$\frac{1}{q_2} = \frac{1}{R_2(z)} - j\frac{\lambda}{n\pi w_2^2(z)}. \qquad \textbf{Equation 47}$$

Equating Equation 46 and Equation 47 yields

$$\frac{C + D(1/q_1)}{A + B(1/q_1)} = \frac{1}{R_2(z)} - j\frac{\lambda}{n\pi w_2^2(z)}. \qquad \textbf{Equation 48}$$

For a beam passing through a thin lens and propagating in air a distance z, the ABCD matrix is

$$\begin{bmatrix} A & B \\ C & D \end{bmatrix} = \begin{bmatrix} 1 & z \\ 0 & 1 \end{bmatrix} \begin{bmatrix} 1 & 0 \\ -1/f & 1 \end{bmatrix} = \begin{bmatrix} 1 - z/f & z \\ -1/f & 1 \end{bmatrix}, \qquad \textbf{Equation 49}$$

where f is the focal length of the objective lens.

It is important to note that the lenses used do not necessarily fit the requirement for the use of the thin lens equation. It is understood that the values calculated using this method are estimations, and that the trend they show in divergence angles as the magnification of the objective lens is increased is far more important than an exact determination of beam divergence. The trend in angles is of more interest than exact values because it was hypothesized that as the divergence angle is increased the linear data sets will converge to an angle dictated by the detecting fiber's NA. These theoretical calculations serve the purpose of showing what trend in divergence angles is expected for the data collected from scattered beam measurements. The hypothesized convergence trend in data collected using the linear scan path is discussed in Section 4.4.

The initial complex beam parameter, q_1, was determined by assuming that the beam was collimated and therefore

$$R(z_1) = \infty. \qquad \textbf{Equation 50}$$

Using q_1 to calculate q_2 and solve for the position of the beam waist after the beam passes through the lens (assuming the lens is located at $z = 0$) was found to be

$$z_m(f, n, w(z_1), \lambda) = \frac{f n^2 \pi^2 w(z_1)^4}{n^2 \pi^2 w(z_1)^4 + f^2 \lambda^2} mm. \qquad \textbf{Equation 51}$$

The beam width, w, was found to be

$$w(f, n, w(z_1), \lambda, z) = \frac{\sqrt{f^2 n^2 \pi^2 w(z_1)^4 - 2 f n^2 \pi^2 w(z_1)^4 z + n^2 \pi^2 w(z_1)^4 z^2 + f^2 z^2 \lambda^2}}{f n \pi w(z_1)} mm$$

Equation 52

Substituting the position of the beam waist, z_m, Equation 51 into Equation 52 yielded the beam width, which could then be substituted into Equation 40 to solve for the Rayleigh range

$$z_0(f,n,w(z_1),\lambda) = \frac{f^2 n\pi w(z_1)^2 \lambda}{n^2\pi^2 w(z_1)^4 + f^2\lambda^2} mm. \quad \textbf{Equation 53}$$

Equation 52 was substituted into Equation 41 to solve for the divergence angle

$$\theta(f,n,w(z_1),\lambda) = \frac{360\sqrt{n^2\pi^2 w(z_1)^4 + f^2\lambda^2}}{fn\pi^2 w(z_1)} degrees. \quad \textbf{Equation 54}$$

Section 4.3.2 Model of Divergence Angle and Rayleigh Range

For all calculations the beam width, $w(z_1)$, used was measured experimentally and found to be

$$w(z_1) = 1.001mm, \quad \textbf{Equation 55}$$

and the wavelength of the laser was 632.8 nm (He-Ne laser). Table 2 lists the values of the input parameters and theoretical results for each of the lenses. The lenses are listed by their magnification and in which medium the detecting fiber was submerged. Two of the data sets were taken in water for the purpose of creating more data sets with the limited number of objective lenses available, but also to verify that measurements could be taken in a medium other than air. The input values used to calculate the theoretical beam parameters were the lens focal length, f, and the index of refraction for the experimental medium. The theoretical calculations included: the distance from the lens to the beam waist z_m, the beam width w_0, the Rayleigh range z_0, and the divergence angle θ.

	Input		Theoretical Calculations			
Lens/Medium	f	n	z_m **[mm]**	w_0 **[nm]**	z_0 **[mm]**	θ°
5x/Air	25.4	1	25.34	5116	0.130	4.52
5x/Water	25.4	1.33	25.40	3843	0.098	4.52
10x/Air	16.5	1	16.50	3320	0.055	6.95
10x/Water	16.5	1.33	16.50	2496	0.041	6.95
20x/Air	9	1	9.00	1811	0.016	12.75
40x/Air	4.5	1	4.50	906	0.004	25.49
60x/Air	3.09	1	3.09	622	0.002	37.12
100x/Air	1.75	1	1.75	352	0.001	65.55

Table 2: Input parameters and theoretical results for each lens. The lenses are listed by their magnification and in which medium the detecting fiber was submerged. The input values are the lens focal length, f, and the index of refraction for the experimental medium. The theoretical calculations include: the distance from the lens to the beam waist z_m, the beam width w_0, the Rayleigh range z_0, and the divergence angle θ. For all calculations the wavelength was 632.8 nm (He-Ne laser).

Table 3 lists the approximate measured distance, D_{meas}, from the lenses to the nearest position of the detecting fiber during experimentation and the theoretically determined distance, D_{theory}, from the lenses to the edge of the Rayleigh range, beyond which point the divergence angle of the beam converges and the equations used to calculate the divergence angle considered valid. D_{theory} was calculated

$$D_{theory} = z_m + z_0. \qquad \textbf{Equation 56}$$

All lenses were limited in positioning by the recessed window (shown in Figure 13). Each lens was secured to the optics table by the same lens holder, however the length of each lens dictated how far it could be placed inside the tube of the recessed window of the sample-holding vat. These measurements and calculations verify that all measurements were taken outside the Rayleigh range.

Lens/Medium	D_{meas} [mm]	D_{theory} [mm]
5x/Air	60	25.5
5x/Water	60	25.5
10x/Air	55.1	16.6
10x/Water	55.1	16.5
20x/Air	32.5	9.0
40x/Air	33.4	4.5
60x/Air	25	3.1
100x/Air	25	1.8

Table 3: Rayleigh range verification. Lenses are listed by their magnification and in which medium the detecting fiber was submerged. D_{meas} is the distance measured from the lenses to the nearest detection fiber position. D_{theory} is the theoretically calculated distance from the lenses to the edge of their Rayleigh range. This validates the assumption that all measurements were taken outside the Rayleigh range.

Section 4.3.3 System Physical Limitations

While taking experimental measurements, the input divergence angle was increased by using lenses of increasing magnification. When using the Olympus DPlan100 lens, which had a calculated divergence angle of about 66°, the angle of the beam far exceeded that which was measurable by the system. The detection fiber range of motion was constrained by the allowable bend radius of the fiber as well as the size of the sample vat. Measurements taken using the Newport 60X lens, with a divergence angle of about 37°, were well within the range of the testing apparatus. The physical limitations of the system constrain measurements to be approximately within the range of 0° to 40°. It is possible that range extends as far as 60°, however to ascertain an exact upper limit further experimentation is necessary.

Section 4.4 Linear Data Limitation Calculations

As introduced in Section 4.1.2, we expected that the experimentally determined divergence angles for data taken along the linear scan path would converge toward a limit

dictated by its NA as the input Gaussian beam divergence angle increased. The detection range of the scanning system itself was also limited by the size of the sample vat in which the detection fiber was positioned. While the main goal of this experiment was to determine which scanning path yielded the most accurate measurements, these experiments were also designed to determine if the limits imposed by the size of the detection vat or by the NA of the detection fiber were reached sooner during linear scanning. To this end, the angle to which linear data measurements of divergence angles converge was determined experimentally and computationally and compared. Using a variety of lenses, we also determined an approximate range of divergence angles small enough to be measured within the confines of the sample vat to compare to the divergence angle limit imposed by NA to determine the most obtrusive limitation factor.

The following sections explain the derivation of the theoretical model of expected linear scan-determined divergence angles. This is done by first deriving an NA-dependent coefficient function, $Q[x]$. Mathematical representations of Gaussian beam profiles were multiplied by $Q[x]$ to alter the ideal beam profile to that expected from linear scan data. The modeled beam profiles also include a coefficient derived to account for reflection at the detection surface/sample medium interface based on the index of refraction of the sample medium. The resulting function of expected linear beam profile depends on the position of the detection fiber in relation to the glass window of the sample vat and the input Gaussian beam divergence angle.

A model of the input Gaussian beam was made using the theoretical Gaussian beam parameters calculated for each lens in Section 4.3.2. The model of the expected linear beam profile was combined with the model of the input Gaussian beam to create

plots of the expected, linear scan path-collected beam profiles for various input Gaussian beam divergence angles. From these plots, we calculated theoretical expected divergence angles for linear scan data for each lens. We found that theoretically, divergence angles determined by linear scans would converge to about 26° as input divergence angle is increased. The comparison of theoretical and experimentally measured divergence angles is presented in Section 4.7.

Section 4.4.1 Optical Fiber Numerical Aperture

The NA of the detection fiber determines the maximum scattering angle at which incoming light will be detectable. For all experiments described in this chapter, the fiber used was Newport F-MSC fiber, which is a step index fiber for the wavelength range 500-1100nm, with a 0.37 NA and a 600μm core. NA is defined by the optical fiber's critical angle for total internal reflection. It is derived from Snell's law and depends on the incident angle of incoming light, θ_i, and the refractive indexes of the fiber core n_1, fiber classing n_2, and the surrounding medium, n_0, which was air, water, or liquid tissue phantom in this study. NA, is expressed as

$$NA = n_0 \sin(\theta_i) = \left(n_1^2 - n_2^2\right)^{1/2}. \qquad \textbf{Equation 57}$$

When the detecting fiber scanned beam profiles in air ($n_0 \approx 1$), the limit of the accepting incident angle was 21.7°, as determined by its NA. The cutoff for θ_i is inversely proportional to n_0, and therefore achieves a maximum in air and only decreases as n_0 increases. For example, if the medium surrounding the detecting optical fiber was water, then θ_i would be equal to 16.1°. The angle θ_{NA} represents the angle associated with the NA of the detecting fiber.

Section 4.4.2 Transmission/NA Angular Dependence

Output power from a linear scan will be dependent on the angle of incident light for two reasons: (1) the angular dependence of the NA of the detecting fiber and (2) reflections at the surface caused by an impendence mismatch between the media that form the interface at the surface of the detecting fiber core.

Outside the range dictated by the NA, data cannot be collected by the detector, as illustrated in Figure 19. $Q[x]$ will be the calculation of the factor by which a theoretical Gaussian beam profile must be multiplied to account for the NA of the detecting fiber. The x-axis is also shown in Figure 19 - it represents the axis along which linear experimental scans across the beam profile were taken. All calculations will be derived as a function of the variable x.

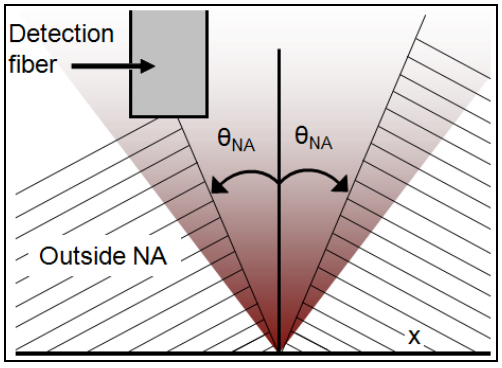

Figure 19: Illustration of the detector's effective range as dictated by the NA of the detecting fiber, θ_{NA}. The fiber is assumed to move in a linear path along the direction of the arrow, wherein the detection surface of the fiber is kept parallel to the x-axis.

Section 4.4.3 The NA Dependent Coefficient Function Q[x]

As the optical fiber scans a beam profile it moves through three mathematically significant regions. Each of these regions is considered individually because the fiber core diameter was a large fraction of the beam diameter, and therefore the shape of the

detection surface must be included in the calculation. The beam, when collimated as it was for several of the experiments in this study, was approximately 1 mm in diameter, while the fiber had a 0.6 mm diameter core. The regions include:

(i) where the fiber core falls entirely within θ_{NA}, and therefore is capable of detecting all incident light:

$$\mathrm{Q[x]} = 1 \text{ and } |\mathrm{x}| \le h\mathrm{Tan}(\theta_{NA}) - d/2, \qquad \textbf{Equation 58}$$

where d is the diameter of the fiber core and h is the distance between the fiber's detecting surface and the source. See Figure 20 (i) for illustration.

(ii) where the fiber core falls entirely outside of θ_{NA}, and is therefore unable to detect any incident light. This is represented by

$$\mathrm{Q[x]} = 1 \text{ and } |\mathrm{x}| \ge h\mathrm{Tan}(\theta_{NA}) + d/2, \qquad \textbf{Equation 59}$$

where d and h are as defined for region (i). See Figure 20 (ii) for illustration.

(iii) Where the detecting surface area of the fiber core is split such that a portion of it can accept light while the other portion cannot because it has moved beyond the NA-inducted limit. See Figure 20 (iii) for illustration.

In this area the function $Q[x]$ is equal to the ratio of the light accepting area of the fiber, A, to the total surface area of the fiber, A_{tot}.

$$\mathrm{Q[x]} = \frac{A[a]}{A_{tot}}, \text{ where } \mathrm{A}_{tot} = \pi\left(\frac{d}{2}\right)^2 \text{ and } A[a] = \int_{-d/2}^{a} \sqrt{(d/2)^2 - x^2}\, dx, \qquad \textbf{Equation 60}$$

where a is the distance from the trailing edge of the fiber (closest to the center line of beam propagation) to the position of the boundary dictated by the NA of the fiber, across which the fiber is unable to detect light. This variable is illustrated in Figure 21. In terms of x, a can be written

$$a = h\mathrm{Tan}(\theta_{NA}) - x\,. \qquad \textbf{Equation 61}$$

By combing Equation 60 and Equation 61, an expression for $Q[x]$ in region (iii) can be written as

$$\mathrm{Q[x]} = \frac{2}{\pi(d/2)^2}\int_{-d/2}^{h\mathrm{Tan}(\theta_{NA})-x}\sqrt{(d/2)^2 - x^2}\,dx\,. \qquad \textbf{Equation 62}$$

$Q[x]$ will be incorporated into a more complete treatment of a modeled Gaussian beam in subsequent sections.

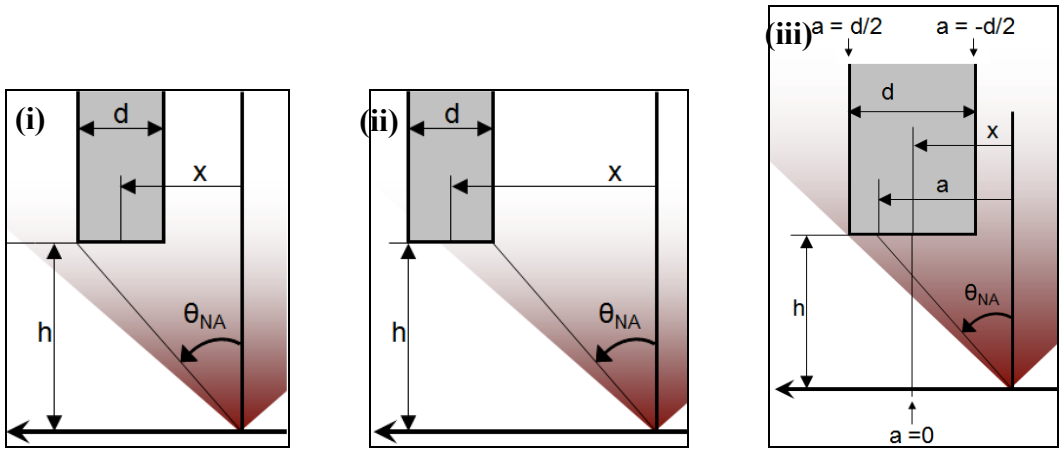

Figure 20: Illustration of the three regions, labeled (i), (ii) and (iii), considered in the derivation of the factor by which the theoretical Gaussian beam profile must be multiplied to account for the NA of the detecting fiber. d is the diameter of the fiber, h is the distance between the source and the fiber, θ_i is the angle between the center of the fiber and the source, and x is the horizontal distance between the center of the fiber and the center of beam propagation.

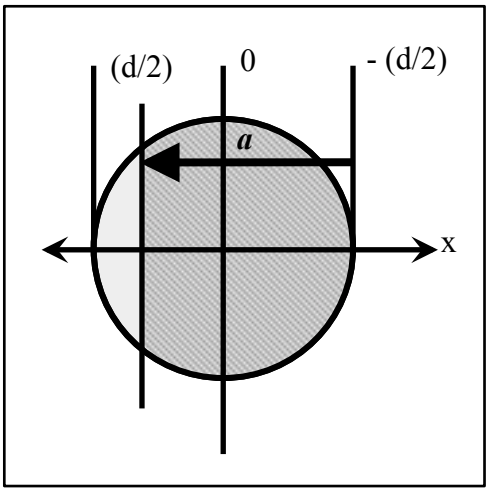

Figure 21: Illustration of the variable a. The circle represents the detecting surface of the fiber; the shaded region is the portion of the fiber that can detect light. The area that is not shaded represents the portion of the fiber that has passed the barrier dictated by the NA of the fiber. The variable a is defined as the distance from the trailing edge of the fiber to this barrier.

Section 4.4.4 Transmission Coefficient Functions

The transmission coefficients for parallel, T_{para}, and perpendicular, T_{perp}, polarizations were derived in Section 3.2:

$$T_{para} = \alpha\beta\left(\frac{2}{\alpha+\beta}\right)^2 \qquad \textbf{Equation 63}$$

$$T_{perp} = \frac{4\alpha\beta}{(1+\alpha\beta)^2} \qquad \textbf{Equation 64}$$

where $\alpha \equiv \frac{Cos(\theta_T)}{Cos(\theta_i)}$ and $\beta = \frac{\mu_1 n_2}{\mu_2 n_1}$. **Equation 65**

Both equations are in terms of α and β. To scale the modeled Gaussian beam by a factor proportional to the transmission coefficient, α must be written in terms of x; but α is dependent on the angle of incidence on the fiber detection surface, θ_i, and the angle of light transmitted to the fiber core, θ_T. In terms of x, these are:

$$\theta_i[x] = Tan^{-1}(x/h) \text{ and } \theta_T[x] = \frac{n_1}{n_2} Sin(\theta_i) = \frac{n_1}{n_2} Sin\left[Tan^{-1}(x/h)\right] \quad \textbf{Equation 66}$$

These equations can be substituted into the equation for α, which can be substituted into the equations for the transmission coefficients, resulting in transmission coefficients in terms of x, resulting in coefficients $T_{para}[x]$ and $T_{perp}[x]$.

Section 4.4.5 Resultant Angular Dependence

The final equation for a Gaussian beam profile equation that incorporates NA and transmission correction coefficient functions has the form:

$$Gaus_{pol}[x] = \begin{cases} G[x] \cdot T_{pol}[x] & 0 < |x| \le hTan(\theta_{NA}) - d/2 \\ G[x] \cdot Q[x] \cdot T_{pol}[x] & hTan(\theta_{NA}) - d/2 < |x| < hTan(\theta_{NA}) + d/2 \\ 0 & |x| \ge hTan(\theta_{NA}) + d/2 \end{cases} \quad \textbf{Equation 67}$$

where $G[x]$ is a Gaussian function with parameters calculated based on experimental observations, $Gaus_{pol}$ is the equation for either polarization, parallel and perpendicular, depending on which transmission coefficient, T_{pol}, is chosen, h is the distance from the source to the detector, d is the diameter of the detecting fiber, and θ_{NA} is the boundary angle dictated by the numerical aperture of the detecting fiber. Equation 67 is valid for sources radiating with divergence angles larger than is limited by the NA of the fiber. However if the relative angle between the source and the detecting surface of the fiber is reduced, i.e. reducing θ_i to approximately match the source angle would correct the NA induced system limitations, thus negating the need for this equation, which is the driving motivation behind testing a rotational scan path rather than a linear scan path.

If the beam is collimated, the only factor that needs to be included is T_{pol}. The calibration that accounts for the effect of this factor, for collimated and divergent beams, is discussed in Chapter 3.

Equation 67 was used to calculate the expected theoretical linearly scanned beam profiles. Figure 22 shows plots of the idealized beam profiles (dashed lines) for various input Gaussian beam divergence angles, θ. For the same angles, plots are also included of the associated expected linearly scanned beam profiles (solid lines). For a divergence angle of 15°, which is much lower than the limit dictated by the NA of the detection fiber (this limit is discussed below in association with Figure 23), the expected beam profiles nearly matches the ideal beam profile, excepting a slight reduction in maximum power due to reflection at the detecting fiber/sample medium interface. These reductions in maximum power are independent of divergence angle. For a divergence angle of 25° the expected beam profile is somewhat limited by the NA of the detecting fiber. For a divergence angle of 35° the expected beam profile shows extreme deviation from ideal.

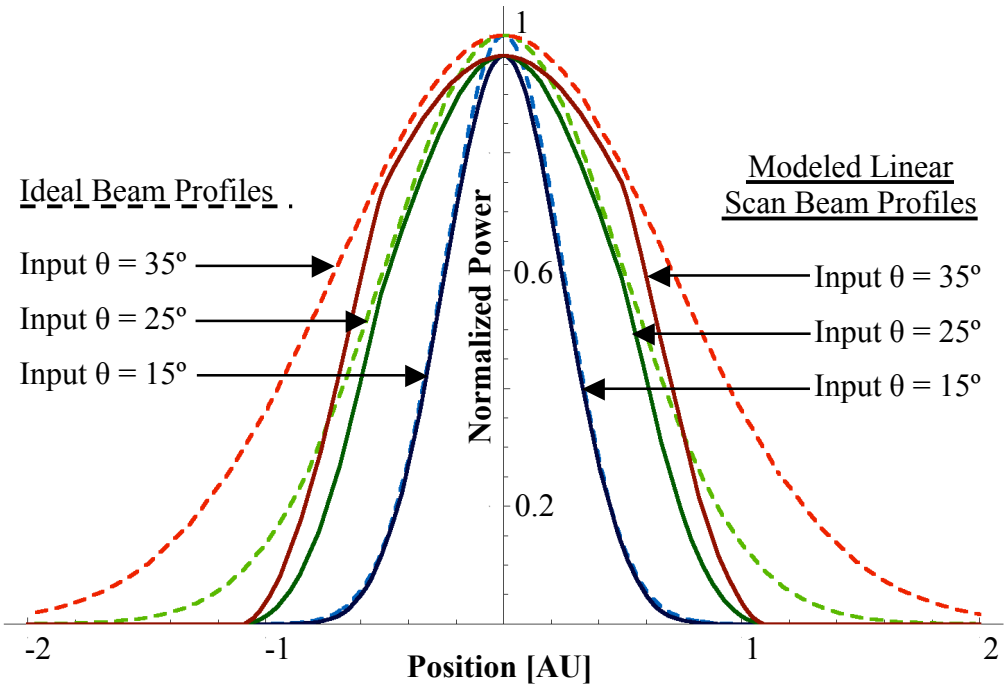

Figure 22: Variations in expected linearly scanned beam profiles by input divergence beam angle, θ. For each modeled input divergence beam angle a dashed line plots an ideal beam profile and a solid line plots the expected linearly scanned beam profile.

As input beam divergence angle increases, the deviation from ideal of the beam profiles also increases, and therefore the divergence angle determined using measurements taken from the beam profiles diverge from ideal. An ideal determination of divergence angle would give results that exactly match the input beam divergence angle. Figure 23 is a plot showing the deviation of the expected divergence angle determined using a linear scan path (solid line) from the ideal divergence angle (dashed line). Calculations showed that the divergence angles determined by linear scans should converge as input divergence angle increased to approximately 26º.

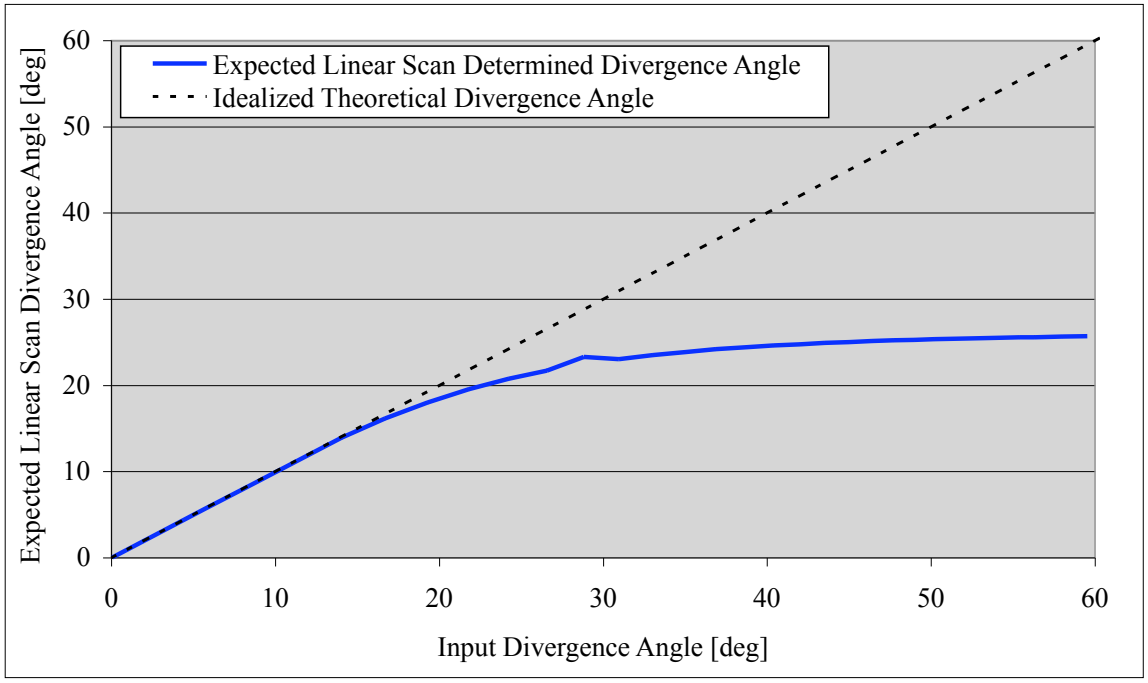

Figure 23: Variation from ideal divergence beam determination due to linear scan system limitations as a function of input Gaussian beam divergence.

Experimental linear scan-determined divergence angle data was compared to the theoretical calculations of expected divergence angles for the purpose of assessing the effects of NA-induced system accuracy limitations in Section 4.7. Experimental data was also used to determine system limitations due to range of motion restrictions. These limitations are discussed in Section 4.3 in conjunction with the theoretical calculations of input divergence beam angles provided by the lenses. In that section we determined that the system was capable of imaging beam profiles of beams with input divergence angles of up to about 40° (and perhaps higher), but no higher than 66°. By comparison, linear scan measurements are expected to converge to about 26°. It is apparent from the theoretical and experimental information discussed thus far that the accuracy of the system, when using a linear scan path, is limited dominantly by the NA of the detection fiber rather than by physical constraints. These factors will be further discussed in

Section 4.7 in terms of the observed convergence of linear scan determined divergence angles.

Section 4.5 Rotational Data Conversion

Rotational scan measurements were taken in increments of degrees. To determine dose from rotational scan data, the angular values were converted from degrees to units of length. This conversion also allowed for easy comparison between linear and rotational data sets.

Section 4.5.1 Rotational Scan Pivot Point Determination

Determining the position of the rotational scan pivotal point in relation to the detection fiber position was the first step in deriving a conversion for rotational data. Figure 24 shows the position of the detection fiber and its geometrical relationship to the detection vat (of which only the thin glass window is shown) and the rotational scan pivotal point. The thin glass window was the reference surface used for all measurements. The fiber was positioned in contact with the thin glass window at the start of all experiments, and this position was referred to as the zero distance position along the direction of propagation. The distance, d, is the measured position of the detection fiber in terms of distance from the glass window. Furthermore, the fiber was positioned so that the center of the scan path coincided with the center of the beam (the maximum measured peak power). In Figure 24, the solid line arrow shows the path of the rotational scan, which followed a circular path around a pivot point. The angle θ represents the angle traversed by the detection fiber, which contains $1/e^2$ of the maximum amplitude of the measured power: this is the beam width in units of degrees. The distance α between

the pivotal point of the rotational scan and glass was unknown and therefore determined experimentally.

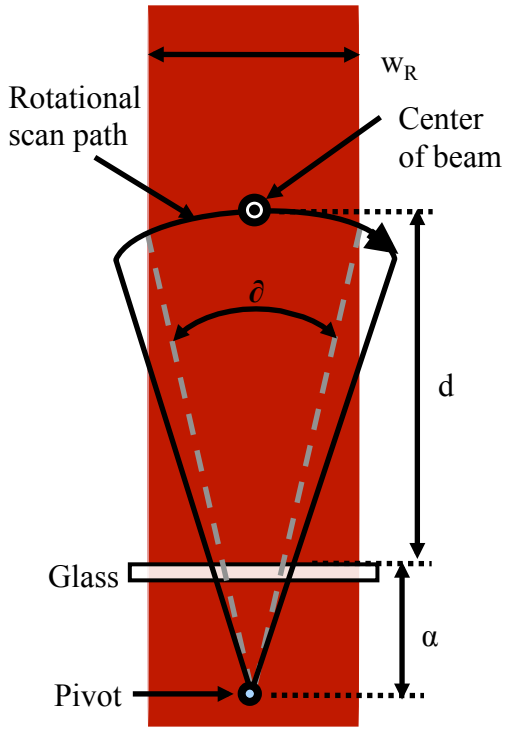

Figure 24: Rotational scan system geometry. The detection fiber was centered on a collimated beam at a distance d from the surface of the thin glass window. The rotational scan path moves the detection fiber along a circulator path around a pivot point. α is the distance between the pivot point and the surface of the glass from which the fiber position was measured. The angle, ∂, represents the angular distance encompassing the collimated beam width, w_R.

NA only limits linear scanning when taking measurements of scattered light. For this reason, linear scans of collimated beams are assumed to be accurate. To determine the distance α, linear and rotational scans of a collimated beam were taken at various intervals, distances d, along the direction of beam propagation. The linear scan data was used to determine the beam width, w_L. Given the experimentally determined beam width, w_L, in units of length, the rotational data was used to calculate α

$$\alpha = \frac{w_L/2}{Sin(\partial/2)} - d. \qquad \textbf{Equation 68}$$

Table 4 lists the values for w_L measured for a collimated beam. Table 5 lists values of α found using the measurements of w_L and the rotationally measured d and ∂.

Linear Data	
Data Set	w_L **[um]**
1mm	1002
2mm	999
3mm	997
4mm	1000
5mm	1004
6mm	1001

Average	1001 ±2

Table 4: Beam width, w_L, measured at various distances d.

Calculation of α	
Data Set	α **[um]**
1mm	540
2mm	468
3mm	448
4mm	428
5mm	404
6mm	414

Average	450 ±50

Table 5: Values of α determined using linear and rotational scan measurements of a collimated beam.

It was apparent from the large standard deviation in α values that it could not simplified to a single constant. As such, the value of α was determined to be best described in terms of a function of distance d, rather than a constant. Fitting a line by least squares to the values of α yielded

$$\alpha[mm] = -24.116d - 534.7. \qquad \textbf{Equation 69}$$

Figure 25 is the graph of α vs. d plotted with the function of α in terms of d and the associated correlation coefficient, R^2. The correlation coefficient is sufficiently high to support the conclusion that α is not a function of d rather than a constant. This is most likely attributable to minor misalignments of the system such that the line between the rotational pivot point and the zero angle measurement position was not perfectly aligned with the central axis of the beam.

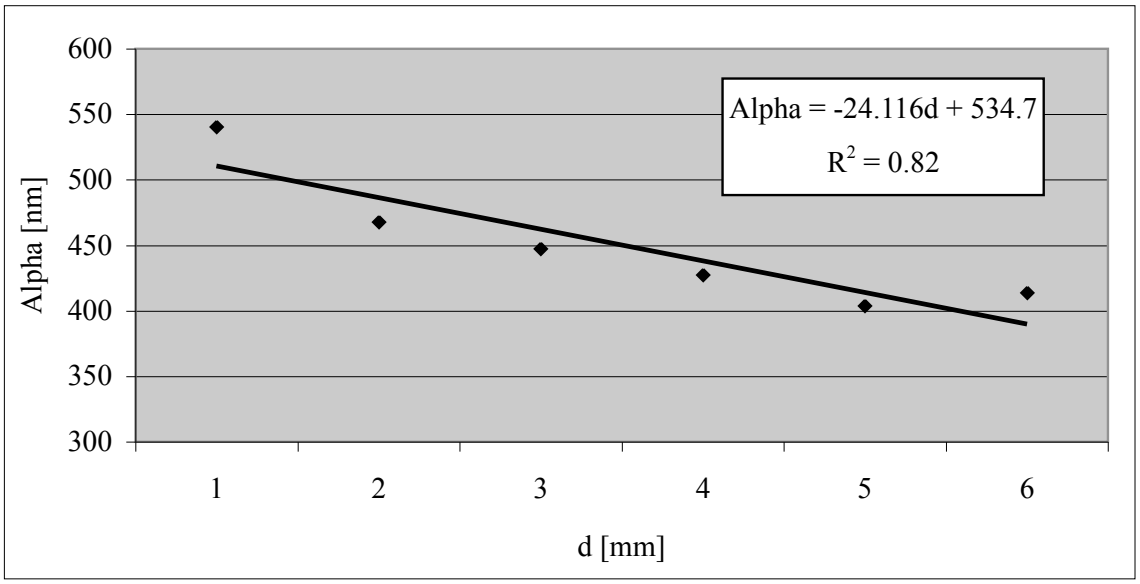

Figure 25: α vs. d plotted with the function of α in terms of d and the associated correlation coefficient, R^2.

Section 4.5.2 Rotational Data Conversion from Units of Angle to Length

The rotational conversation can be derived based on experimental measurements, including the determination of the rotational pivot point described in the previous section. Figure 26 illustrates the geometry of the system set-up, which includes a scattered beam, and the parameters involved in the calculation of a linear projection of the rotational data. Neither scan path data type was assumed to be accurate for this experiment. The system alignment was not altered between experiments so that the function for α, determined in the previous section, remained valid. The goal of this conversion is to project the measurements taken along the curved line of the rotational scan path to a linear line located at the beam width. This linear line is the beam width used for determining the divergence angle of the beam for rotational scans and is labeled w_R in Figure 26. Data points taken along the rotational scan path have an angular coordinate, β, which is converted to a distance b so that the measured power at point p_R, which lies on the rotational scan path line, is projected onto w_R to the position p_p. The projection, w_R, converts the position of all the rotational data points for the purpose of plotting linear and rotational data sets together. The total length of w_R was used to compare trends in measured divergence angles of each scan type as the divergence angle of the beam increased.

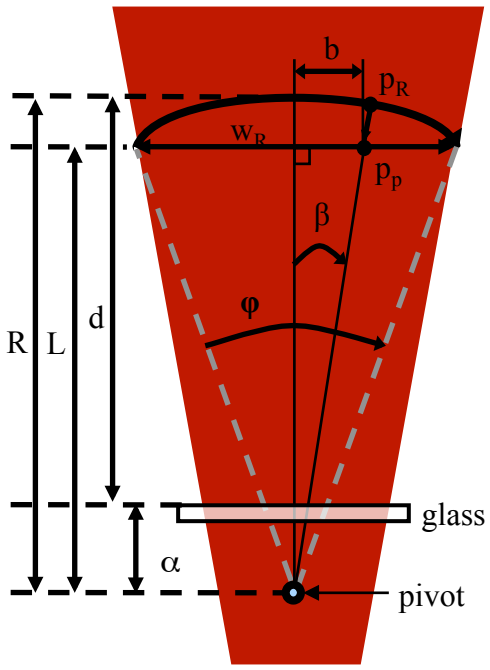

Figure 26: Parameters and system geometry used to calculate a linear projection of the rotational data (along the curved scan path line) to the line w_R. The distance d and angle ∂ were measured experimentally. ∂ represents the angle subtended by $1/e^2$ of the maximum profile power as measured rotationally. The function for the distance α was determined in a separate experiment. The rotational scan path radius, R, which depends on d and α, and the distance L, which depends on ∂ and R, were used to convert the measured angular parameter β, to the distance b. This converstion effectively translated the position of each measured power reading. For example: the power reading measured at point p_R was moved to the position p_p. The straight line w_R, represents the beam profile in the form: power [AU] vs. position [nm].

The width of the beam, w_R, is

$$w_R = 2R\mathrm{Sin}\left(\frac{\partial}{2}\right), \qquad \textbf{Equation 70}$$

where ∂ is the angle subtended by $1/e^2$ of the maximum power of the beam profile as measured rotationally and R is radius of the rotational scan path.

$$R = d + \alpha, \qquad \textbf{Equation 71}$$

where the value of d is measured for each data set and α is dependent on d according to Equation 71. The length, L, represents the distance along the axis of beam propagation

from the rotational pivot point to the position of w_R. L depends on ∂ and w_R and, like R and α, is therefore calculated for each data set (position d).

$$L = \frac{w_R}{2}\mathrm{Tan}(\frac{\partial}{2}). \qquad \textbf{Equation 72}$$

From Equation 72 the converted position of each rotational data set to its position on the projected line w_R is

$$b = L\mathrm{Tan}(\frac{\partial}{2}). \qquad \textbf{Equation 73}$$

The projection of the rotational data along w_R allows linear and rotational data sets to be compared visually on the same plot. The total length of w_R, taken from several data sets, was used to determine the divergence angle of the beam for each beam scattered by a lens, measured using a rotational scan path. The divergence angle determined using linear and rotational scan paths are compared to theoretical calculations in Section 4.7.

Section 4.6 Measured Divergence Angle

Divergence angles of a beam scattered through various lenses were determined from measurements taken along linear and rotational scan paths for the purpose of comparing the experimental scan type measuring techniques, wherein the rotational data was converted to a linear projection as described in Section 4.5. Figure 27 shows an example measurement of divergence angle, which relies on beam width measurements of the beam after it is scattered through a lens. For either scan type, the beam profile was measured at distances d_1 and d_2 from the glass of the sample vat, and the beam widths were found to be w_1 and w_2 respectively. The divergence angle was calculated from these measurements as

$$\theta = 2\varphi = 2\mathrm{Sin}^{-1}\left(\frac{w_2 - w_1}{2\sqrt{\left(\{w_2 - w_1\}/2\right)^2 + \left(d_2 - d_1\right)^2}}\right), \qquad \textbf{Equation 74}$$

where φ is the divergence half-angle.

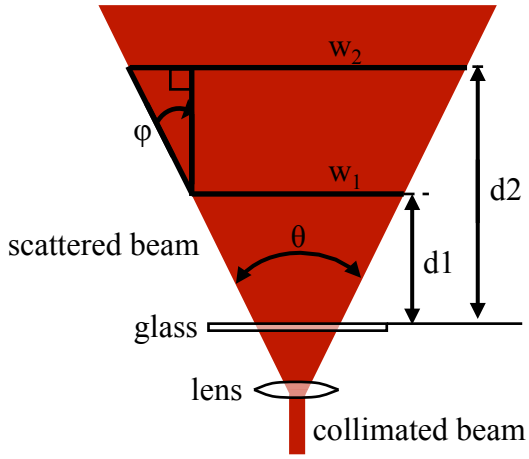

Figure 27: Geometry and parameters used to determine divergence angle. The divergence half angle, φ, was determined using beam profile width measurements, w_1 and w_2, taken of a beam scattered through a lens at interval distances from the sample vat glass, d_1 and d_2.

Section 4.7 Comparison of Experimental and Theoretical Data

One-dimensional Gaussian beam profiles were imaged across the center of a laser beam scattered by various lenses and were used to determine optimal system parameters by testing the accuracy of dose measurements made using said profiles. The experimental set-up and procedure were described in greater detail in Section 4.2. Parameters that varied during this experiment included:

Scan path: linear or rotational
Input beam divergence: θ, via variations in lens magnification
Sample medium: air or water, in which the detection fiber was submerged
Distance: d, the scan center position along beam propagation axis

The beam profile measurements, taken at various distances, d, along the direction of beam propagation, were used to determine beam width. The scan path followed by the

detection fiber was either linear or rotational. The linear scan path, the more simple path choice for implementation and measurement extraction, allowed the detection surface of the fiber to remain perpendicular to the direction of beam propagation as it imaged each beam profile. However, the linear scan path was hypothesized to be limited in detection range by the NA of the fiber. A rotational scan path allowed the detection surface of the fiber to change orientation with respect to the angle of incident light from the scattered beam such that its ability to detect light remained unlimited by the fiber's NA. The fiber rotated about a pivot point located at the zero position shared by both scan paths. Rotational position data, originally taken in units of angle, was converted to units of length by the process discussed in Section 4.5 before beam width measurements were made. Linear position data was originally taken in units of length and therefore beam widths were measured directly from linear profile scans.

Using several different objective lenses and two different sample media, air and water, allowed us to vary the input beam divergence angle. The theoretical calculations associated with these lenses are discussed in Section 4.3. In the following figures, the data is labeled according to the magnification of the lens and the sample media used when the data was taken. In the case where theoretical information is presented below, the calculated value was determined using parameters for the lens and media by which it is labeled.

Figure 28 shows the experimentally determined beam widths taken for each lens magnification and sample medium combination listed by the measured distance, d, at which each measurement was taken. The distance, d, represents the distance between the

glass window of the sample vat (zero position) and the position of the optical fiber detection surface along the axis of beam propagation.

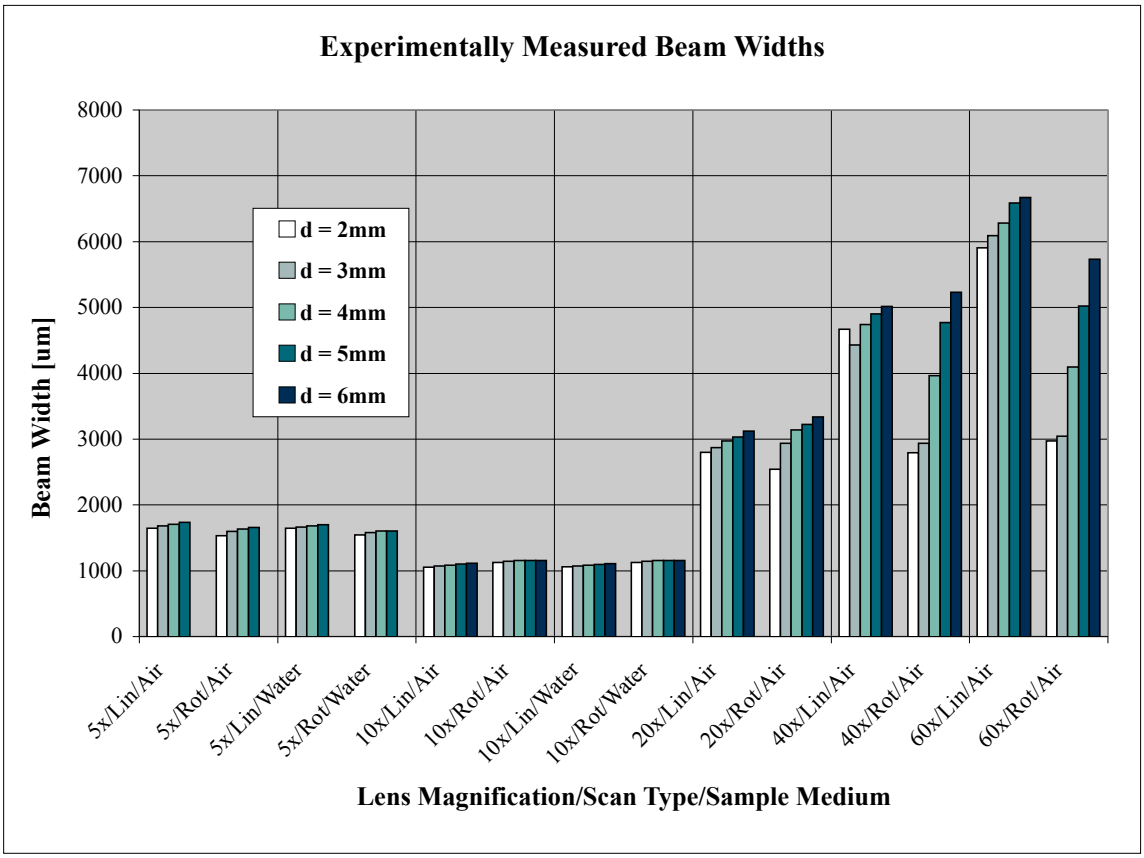

Figure 28: Experimentally determined beam widths that were measured at $1/e^2$ of the peak power of each beam profile for linear (Lin) and rotational (Rot) scan types, at a distance, d, from the sample vat glass window, for various lens magnifications and sample media.

Measurements of the divergence angle were taken by comparing two beam width measurements per calculation. Figure 30 shows the geometry dictated by the experimental set-up considered in the measurement of the divergence half-angle, φ, which depends upon beam width measurements, w. Figure 29 and Figure 31 show the measurements of the divergence angle for each scan type, wherein $\theta = 2\varphi$ and θ1 is the determined using φ_1, θ2 is the determined using φ_2, and so on.

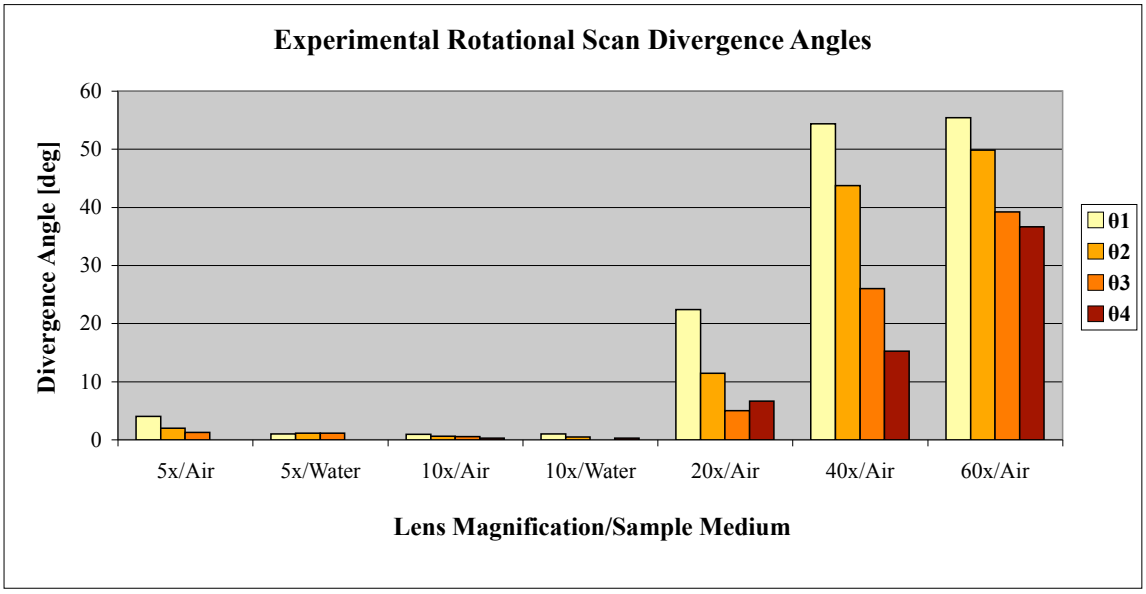

Figure 29: Experimental rotational scan determined divergence angles, θ, for various detection fiber positions, lens magnifications, and sample media. Two beam widths, w_n and w_{n+1}, taken at distance d_n and d_{n+1} from a reference plane were used to calculate θn.

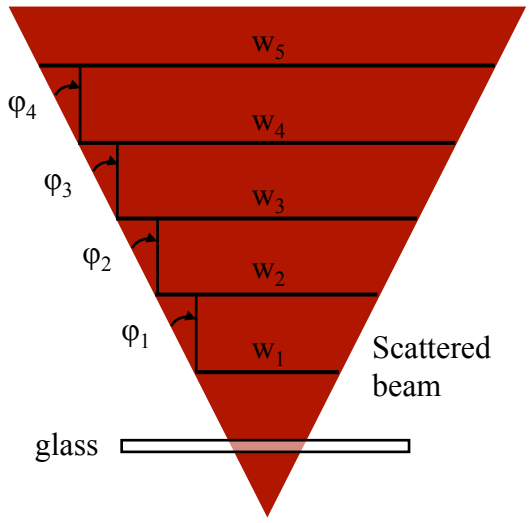

Figure 30: Geometry and parameters used to determine divergence angle wherein the divergence half angle, φ_n, depends on measurements of beam widths w_n and w_{n+1}.

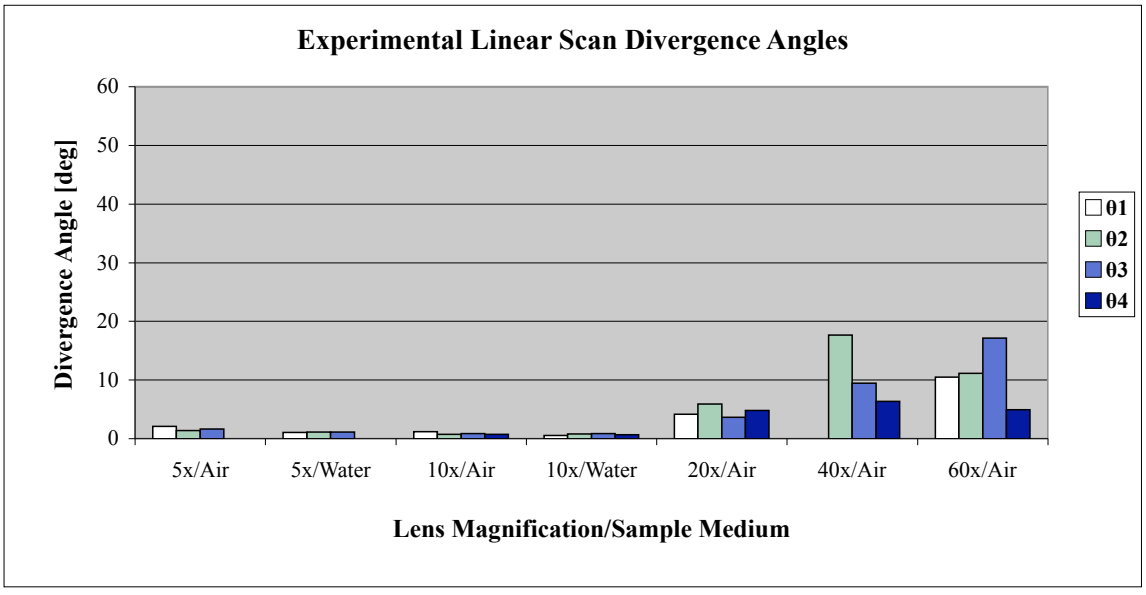

Figure 31: Experimental linear scan determined divergence angles, θ, for various detection fiber positions, lens magnifications, and sample media. Two beam widths, w_n and w_{n+1}, taken at distance d_n and d_{n+1} from a reference plane were used to calculate θn.

Figure 32 compares the experimentally determined divergence angles for each scan type averaged for each data set (lens magnification and sample media). It can be seen in this figure that linear and rotational angles were similar for lenses of lower magnification power, which corresponds to a smaller input divergence angle. However, as the input divergence angle increased, linearly and rotationally determined measurements diverged, as was hypothesized. It is clear that these two scan types do not yield equally accurate measurements. These values are compared to theoretical calculations of input divergence beam angles for each data set based on lens and sample media parameters in Figure 33 for the purpose of determining which scan path results in the most accurate measurements.

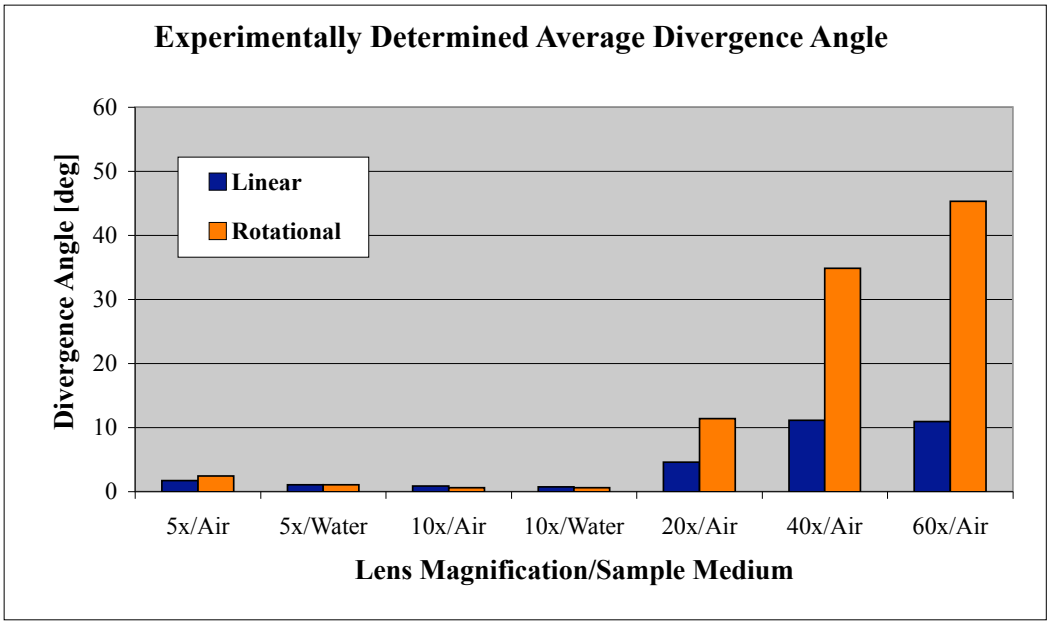

Figure 32: Average experimental divergence angle for each data set from linear and rotational data compared.

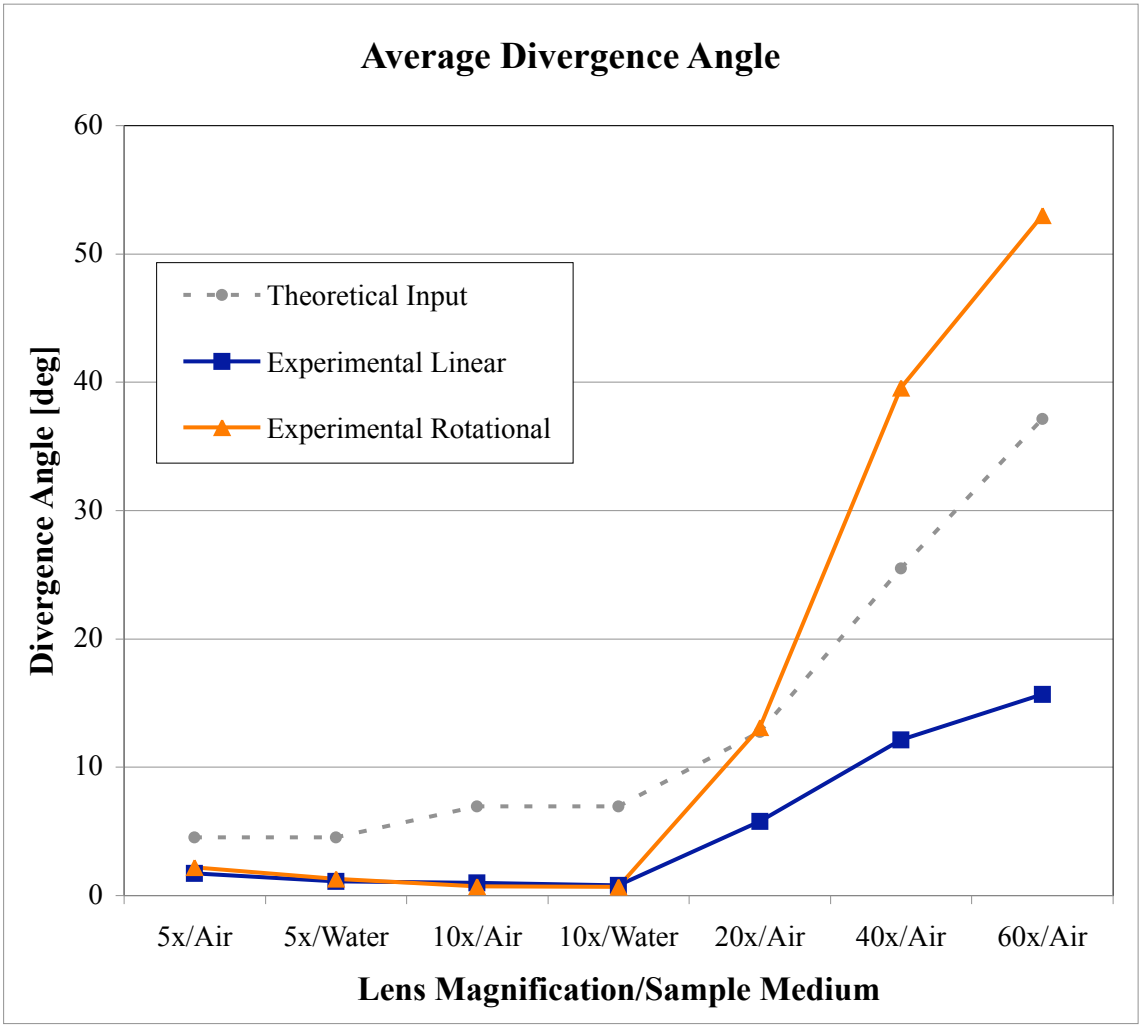

Figure 33: Average experimental divergence angle for each data set from linear and rotational data compared to theoretical input beam divergence angles, listed by scattering lens magnification and sample medium.

It is clear, from Figure 33, that the NA of the detection fiber in fact limits the detection range of linear scanning. In Section 4.4, it was theoretically determined that said limit should be about 26°, but experimentation showed it to be less than 20°. Furthermore, we determined, in Section 4.3, that physical limitation of the system, which was imposed by the bend radius of the fiber and the size of the detection vat, only stipulated that the scattered beam be under about 40°. Obviously the NA induced

limitation would be exceeded well before the physical size of the system imposed detection constraints.

Based on Figure 33, we recommend that the rotational scanning be used for laser therapy dose analysis, as it yields more accurate results than linear scanning. Alternatively, a fiber with a much higher NA, or with compensation optics could be used to circumvent the limitation, if linear scanning is desired. It was not possible to determine the extent by which the rotationally determined divergence angles may have been erroneously skewed by the necessary conversion from angular units to those of length, discussed in Section 4.5. But, even assuming that error was introduced by the conversion, the difference between the accuracy of linear and rotational scan measurements is still large enough to be certain that the rotational scan path is the optimal path.

CHAPTER 5 CONCLUSIONS

We designed and tested a method for measuring sub-dermal OT dose capable of device safety and efficacy verification, the determination of sub-dermal dose safety standards and the study of laser beam propagation through tissue. In Chapter 3 we verified a calibration method usable in various sample media. In Chapter 4 we determined the extent of system limitations due to detector range of motion, optical fiber characteristics and scan path.

Section 5.1 Fiber Optic Detection within Various Sample Media Feasibility and Calibration

The optical fiber we used in experiments was capable of scanning a laser beam profile in sufficient detail to allow for the measurement of beam width, which is essential to the determination of dose. This scanning was successfully completed in air, water and a tissue phantom (fatty emulsion) using only a collimated input beam from a He-Ne laser, which emitted at 632.8nm at a measured total maximum power of 26.7mW with a beam width of about 1 mm. However, direct measurements yield only results in arbitrary units due to the power lost in reflection at the sample media/fiber detection surface interface and attenuation due to bends in the fiber.

To account for all power loss we designed a method of calibration suitable across sample media. The measurement system utilizes an optical fiber as a relay from the scattered beam to a photo detector. This method involved taking measurements, at the same depth, using the fiber and the photo-detector directly and compared the results to determine an intensity function correction factor, F. The total power, A_{tot}, measured

directly by the photo detector (which was large enough to include the entire beam) represents the amplitude of the Gaussian beam measured by the fiber (used to determine the standard deviation, σ). This Gaussian beam function and total power form an intensity function. The product of the correction factor, F, and the peak value measured by the fiber, A_{fiber}, was assumed to be equal to the intensity function integrated over the radius of the fiber core, r_{core}:

$$A_{fiber} \cdot F = 2\pi \int_0^{r_{core}} x \frac{A_{tot}}{2\pi\sigma^2} e^{\frac{-x^2}{2\sigma^2}} dx . \qquad \textbf{Equation 75}$$

Equation 75 was used to determine a universal correction factor F for this optical fiber based detection system. Using this equation we calculated expected values for measurements taken by the photo detector through variously sized apertures. Comparing these values to those determined experimentally, we confirmed the validity of this calibration method. However, a correction factor must be determined for each phantom or tissue sample, source and detector.

Although we were unable to theoretically model all sources of loss, we calculated and confirmed the fraction of loss due to reflection. This confirmation is valuable for future calibrations, for *in-vivo* tissue samples particularly. The method used to determine the correction factor cannot be used *in-vivo* because it would be overly invasive to position the photo detector directly inside living tissue. The only difference between detecting a signal via a fiber in air and in tissue is the reflection coefficient. Therefore, the correction factor actually only needs to be determined experimentally once for a given system (a source, fiber, and photo detector combination). Once completed, only an

estimate of the index of refraction of the tissue would be needed to determine and integrate a reflection loss factor, thus calibrating the system to the tissue.

Section 5.2 Scanning Considerations

The dose measuring system and method we propose requires scanning an optical fiber across a scattered laser beam profile. To determine the optimal path by which to translate the fiber, we considered physical limitations and the beam width measurement accuracy of two different scan path shapes: linear and rotational. Each method presented different limitations, which we weighed against their unique advantages.

Section 5.2.1 Linear Scanning

Linear scanning has the advantage of simple scan geometry. Data taken along this path results in power readings of arbitrary units in position intervals of distance, from which a beam width measurement can easily be taken. The size of the sample vat limits the range of mutation of the fiber and therefore its ability to detect widely scattered beams. However, an optical fiber is also limited in its acceptance angle by its NA. Linear scanning moves the optical fiber such that its detection surface is always perpendicular to the vector of beam propagation. As such, light scattered beyond a certain angle will not be detected by the fiber, regardless of the physical system limitations.

To determine the extent of physical limitations, we imaged beam profiles of laser beams scattered to various divergence angles by various lenses. We theoretically calculated the expected divergence angle of each beam and experimentally determined the same for comparison. The most widely scattered beam was found to have a divergence angle of about 66°, and was too large for either scan path method to completely scan the beam profile due to the restriction imposed by the sample vat size.

The next largest angle, about 37°, was well within the capability of the system to physically translate the fiber through the entire beam profile. The physical limitations of the system constrain measureable scattered beam divergence angles to be approximately within the range of 0° to 40°.

The same experimental measurements were used to determine the NA-imposed acceptance angle limitation. For comparison, we theoretically modeled the expected linearly scanned output beam profiles incorporating a mathematically derived NA limitation. This model predicted that the linearly determined divergence angles would converge to about 26°. Experimental results showed this convergence angle to be less than 20°.

Theoretical and experimental results prove that linear scanning accuracy is limited dominantly by the NA of the fiber rather than by physical constraints. A further drawback to linear scanning is the fact that beam profiles produced by this method result in Gaussian shaped curves, even if part of the profile is outside the range of detection. Therefore, it is impossible to tell from looking at data if a beam divergence angle found to be near 20° is accurate or if the beam is actually much more widely scattered but cut off by the acceptance angle limitation. If linear scanning is used for dose measurements, we recommend the use of a fiber with a very high NA or other measures be taken to mitigate this effect.

Section 5.2.2 Rotational Scanning

Rotational scanning was tested as an alternative to linear scanning, and was designed to mitigate the effect of NA-induced limitations. By translating the fiber along a rotational path centered on the point which the laser beam is incident upon the sample

and simultaneously rotating the fiber, the detection surface of the fiber can be maintained such that the incident angle of the scattered light remain below the critical angle. This would allow the system to detect more widely scattered beams than possible using linear scanning. However, the accuracy of this method is dependent upon the positional data conversion made necessary by its angular scanning geometry. Data taken along this path results in power readings of arbitrary units in position intervals of angle, which must then be converted to distance to determine the beam width.

We derived a conversion factor for rotationally scanned data and verified components thereof. We found that the data could be converted as long as we could determine accurately the position of the rotational axis. We found experimentally that the distance between zero point, the position defined as where the fiber surface touches the glass window of the sample vat, and subsequent fiber detecting surface positions was not a constant. In fact it varied as a function of the distance between the zero point and the detection fiber. Even so, data conversion was possible and was experimentally determined to be accurate by comparing rotationally and theoretically determined divergence angles. We recommend that further iterations of dose measuring systems using rotational scanning include a simple and accurate means by which to determine the function of the rotational axis position each time the optical fiber position is adjusted.

Section 5.2.3 Comparing Linear and Rotational Scan Paths

We also compared linearly, rotationally, and theoretically determined divergence angles for scattered beams produced using various lenses. Based on observations we recommend the use of rotational scanning over linear scanning. Rotational scanning

provides a larger range of accurate beam profile measurements and greater measurement certainty because it is not hindered by fiber NA.

References

[1] F. C. Delori, R. H. Webb, and D. H. Sliney, "Maximum permissible exposures for ocular safety (ANSI 2000), with emphasis on ophthalmic devices," *Journal of the Optical Society of America A*, vol. 24, no. 5, p. 1250, May. 2007.

[2] S. S. Charschan and B. A. Rockwell, "Update on ANSI Z136.1," *Journal of Laser Applications*, vol. 11, no. 6, p. 243, 1999.

[3] M. Wolbarsht and D. Sliney, "Historical development of the ANSI laser safety standard," *Journal of Laser Applications*, vol. 3, no. 1, pp. 5–10, 1991.

[4] D. H. Sliney, "Radiometric quantities and units used in photobiology and photochemistry: recommendations of the Commission Internationale de L'Eclairage (International Commission on Illumination).," *Photochemistry and photobiology*, vol. 83, no. 2, pp. 425-32.

[5] A. Esnouf, P. A. Wright, J. C. Moore, and S. Ahmed, "Depth of penetration of an 850nm wavelength low level laser in human skin.," *Acupuncture & electro-therapeutics research*, vol. 32, no. 1-2, pp. 81-6, Jan. 2007.

[6] P. J. Kolari, "Penetration of unfocused laser light into the skin," *Archives of Dermatological Research*, vol. 277, no. 4, pp. 342-344, 1985.

[7] G. P. Agrawal, *Fiber-optic communication systems*. Wiley-Interscience, 2002.

[8] M. Born and E. Wolf, *Principles of Optics*, Second (re., vol. 12. Oxford: Pergamon Press, 1964.

[9] J. P. Powers, *An introduction to fiber optic systems*. Aksen Associates, 1993.